Abstract

In March 1988 a team from the Radiation Laboratory of the University of Michigan performed field measurements of the backscatter characteristics of snow at millimeter-wave frequencies. This short series of measurements was one of the first operational uses of specialized equipment only recently available to the Radiation Laboratory and served as a practice run for extensive snow experiments planned for the winter of 1988-89. Several types of measurements were made, including the diurnal experiment described in this report.[1]

Contents

List of Figures

List of Tables

1 Introduction

Snow is an important natural resource which is receiving increasing interest in the field of remote sensing. Scientists in hydrology, climatology, agriculture, meteorology, and other disciplines desire increased accuracy in measuring the extent and characteristics of snowpacks on local, regional, and continental scales [1]. Modern developments in remote sensing show much potential in the determination of snow areal extent, snow depth, snow liquid water content, and snowpack structure.

The millimeter-wave portion of the spectrum (30-300 GHz) has not yet been extensively utilized in the remote sensing of snow (compared to centimeter wavelengths and optical frequencies). Further study and additional data are necessary to determine which snow parameters are optimally detected at millimeter-wave frequencies. Our study is designed to help alleviate this shortage of data.

The experiment described in this report was conducted to study the diurnal variation of the radar backscatter from snow. The effects of surface roughness, liquid water content, and other snow characteristics are also considered.

2 Previous Observations

Liquid water content has been found to have a significant effect on the radar backscatter at millimeter-wave frequencies [8,9,10]. In addition, "hysteresis" effects have been observed by Stiles and Ulaby [6], in which the backscatter response leads the liquid water content during the melting stage and lags behind it during the refreezing stage. The sensitivity of radar scattering to liquid water content has been found to decrease with increasing frequency [10], and the radar response saturates at lower values of the liquid water content as the frequency is increased [7].

Surface effects are expected to be significant only for the wet snow case and the work of Williams, Gallagher, *et al.* [8,9,10] supports this. The role of snow crystal size has been investigated with varied results. The snow grain size was found to not be significant for dry snow by Williams *et al.* [8,9], but earlier studies by Williams *et al.* [10] found it to be significant, with σ^0 decreasing as grain size increased.

The goal of this investigation is to examine all of these effects. However, due to the difficulty associated with varying crystal size, the primary parameters examined thus far are liquid water content and surface roughness.

3 Description of Experiment

A team of four researchers from the University of Michigan Radiation Laboratory traveled to Houghton, Michigan, located on the Keweenaw Peninsula of Michigan's Upper Peninsula, during the week of March 27-April 2, 1988. Snow experiments were conducted on March 29, 30, and 31 at a test site adjacent to the Keweenaw Research Center. The experiments included measurement of the radar backscatter from snow as a function of incidence angle (at several polarizations and two frequencies), in addition to a "diurnal" experiment in which the radar backscatter was measured as a function of time over a complete darkness-daylight-darkness cycle. The diurnal backscatter experiment was conducted on March 31.

Figure 1: The MMP system is shown mounted on the boom truck (center) at the Houghton experiment site.

3.1 Equipment

The University of Michigan Millimeter-Wave Polarimeter (MMP) was the primary instrument used in the experiment. The MMP is a scatterometer based on the HP 8510 Vector Network Analyzer. As shown in Figures 1, 2, and 3, the scatterometer antennas are mounted on an extendable boom on a large truck, making measurements of a wide variety of natural targets possible. Like- and cross-polarized backscatter are measured at 401 discrete frequencies over a 2 GHz bandwidth, with center frequencies of 35 and 94 GHz. (A 140 GHz channel has been added since the date of this experiment.) In addition to displaying the spectral response, the inverse-FFT capability of the HP 8510 allows real-time time-

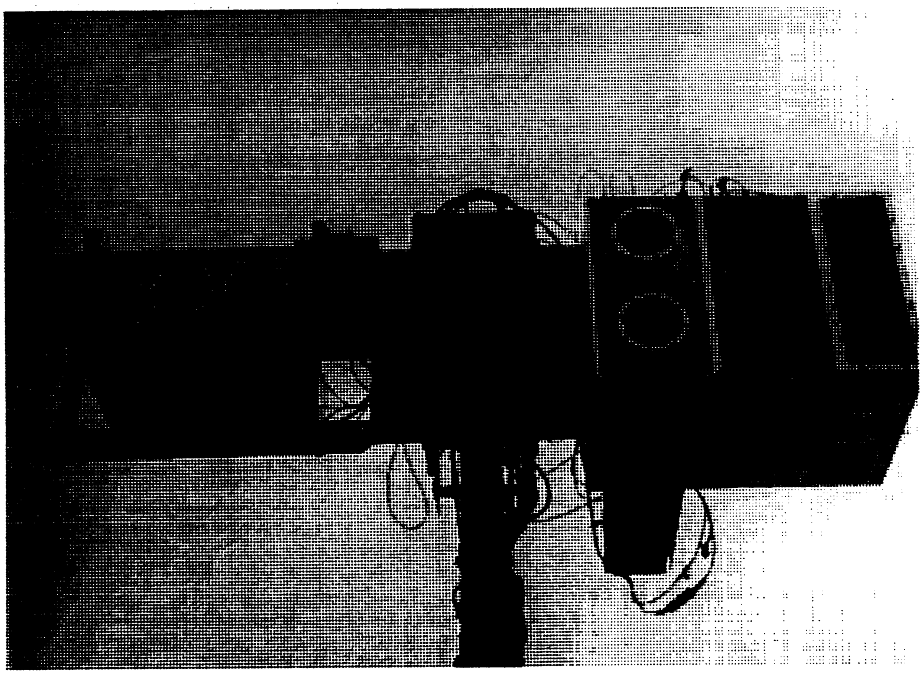

Figure 2: A close view of the sensors mounted on the boom. The radiometers are on the left, and the radars are on the right.

Figure 3: The MMP system is controlled from a shed on the bed of the boom truck. Operators are shown operating the HP 8510 Network Analyzer.

domain analysis. The MMP is described in more detail by Ulaby *et al.* [2].

The original experiment plan included the collection of snow emission data concurrently with the backscatter data using three radiometers with center frequencies of 35, 94, and 140 GHz. However, mechanical failures precluded the use of the radiometers.

3.2 Experimental Technique

Due to a variety of logistical and technical problems, the MMP system was not available for snow measurements until quite late in the winter, thus narrowing the scope of our experiments. However, by preparing the snow surface in various ways, we were able to maximize our experimental opportunities.

3.2.1 Target Preparation

At the date of the experiment (late March), the snow surface was heavily metamorphosed, having gone through numerous melt/freeze cycles. Individual snow crystals were no longer distinguishable, having formed into large icy clumps. A typical sample from the upper surface of the snow is shown in Figure 4.

In order to measure the effect of surface roughness on the backscatter from snow, the snow surface to be measured was divided into three sections, as shown in Figure 5. Preparation of the snow surface areas is shown in Figure 6. A garden rake was used to roughen the surface of the first section, resulting in a "slightly rough" area, with a typical rms surface roughness of 0.880 cm (Figures 7 and 8). The second section was left undisturbed and will be referred to as "smooth" snow. Its rms surface roughness was 0.488 cm (Figures 9 and 10). Several people walked

Figure 4: A typical sample from the upper surface of the snowpack. The snow crystals are heavily metamorphosed.

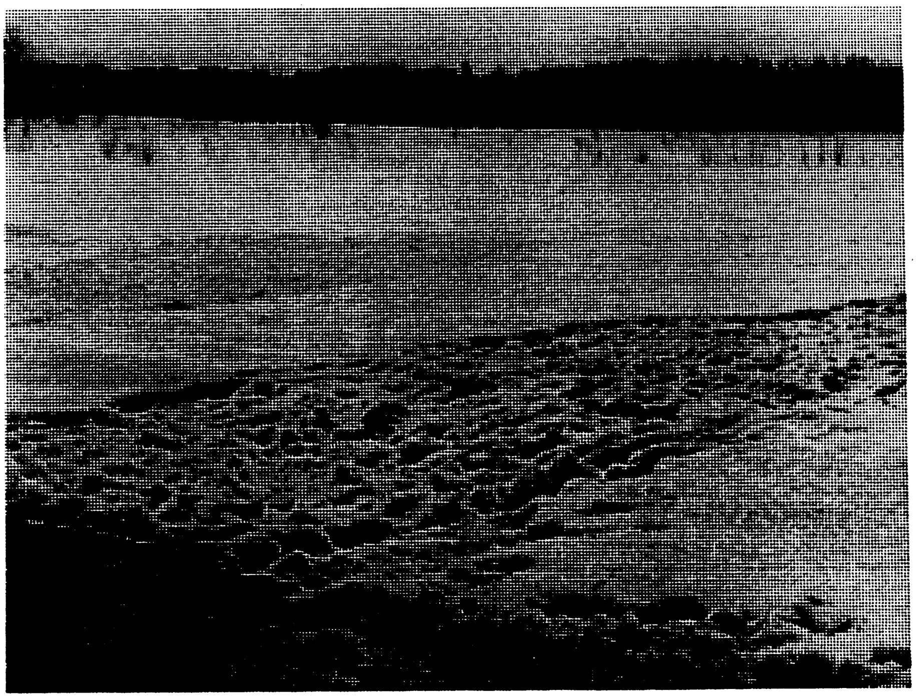

Figure 5: The target area was divided into three areas; the surface in each area was prepared differently. The "very rough" surface area is in the foreground.

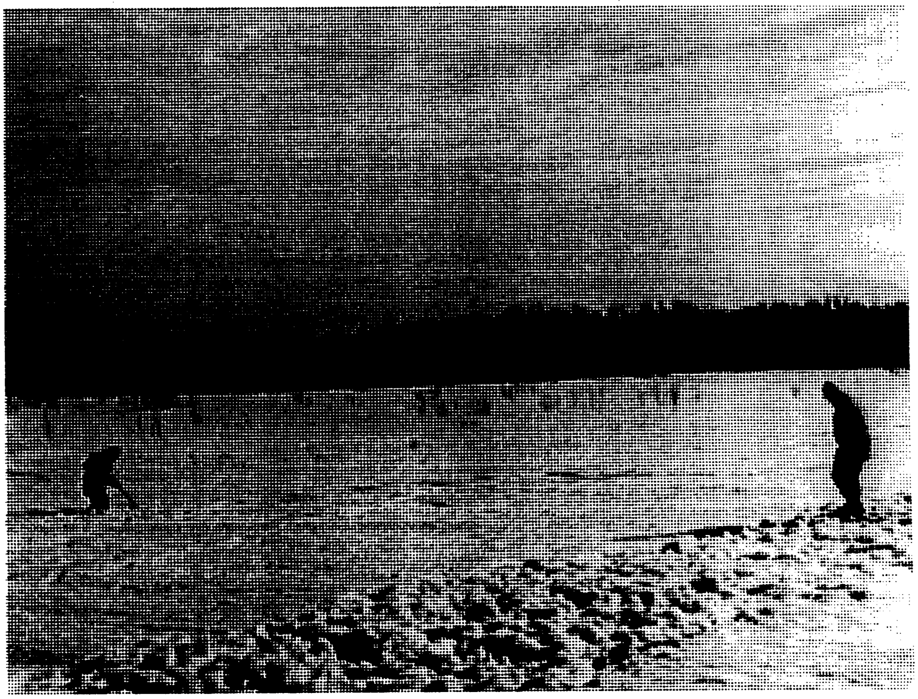

Figure 6: Snow in the "slightly rough" surface area (left) was raked with a garden rake. The "very rough" surface area (right) was walked through repeatedly. The undisturbed surface area is in the center.

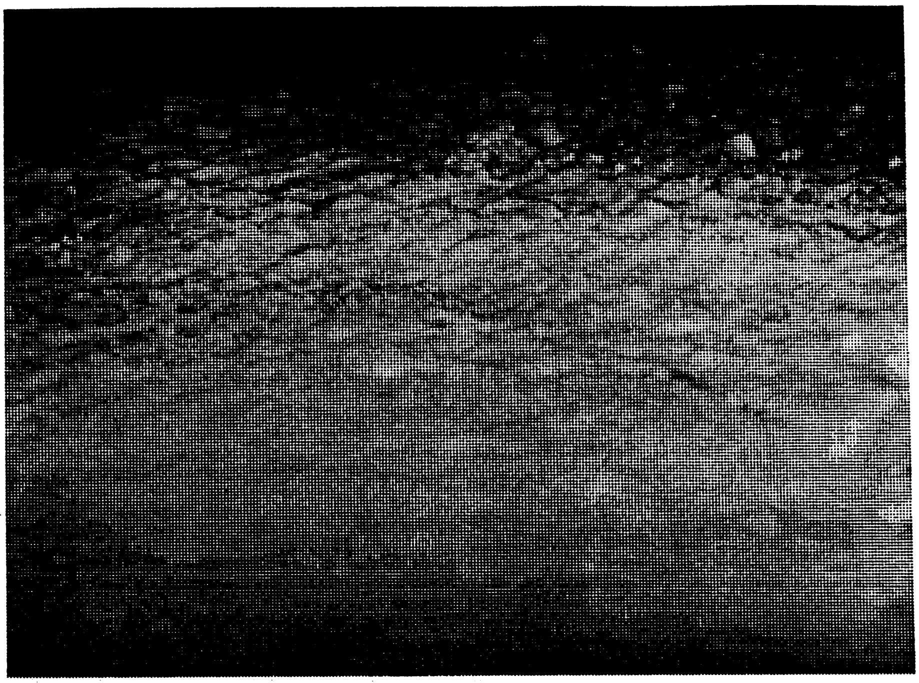

Figure 7: "Slightly rough" snow surface

through the third section, which will be designated "very rough" snow. Its typical rms surface roughness was 1.976 cm (Figures 11 and 12).

3.2.2 Calibration

A 38.1 cm (15-inch)-diameter aluminum sphere mounted atop a cylindrical styrofoam pedestal was used as a calibration target, as shown in Figures 13 and 14. The calibration was performed in the time domain; i.e., the time-domain response of the sphere was integrated to give the total power returned from the sphere in the 2 GHz bandwidth. The system constant K was determined using this result, the range to the sphere, and the known radar cross section of the sphere. Separate system constants were obtained for each frequency and polarization. The entire

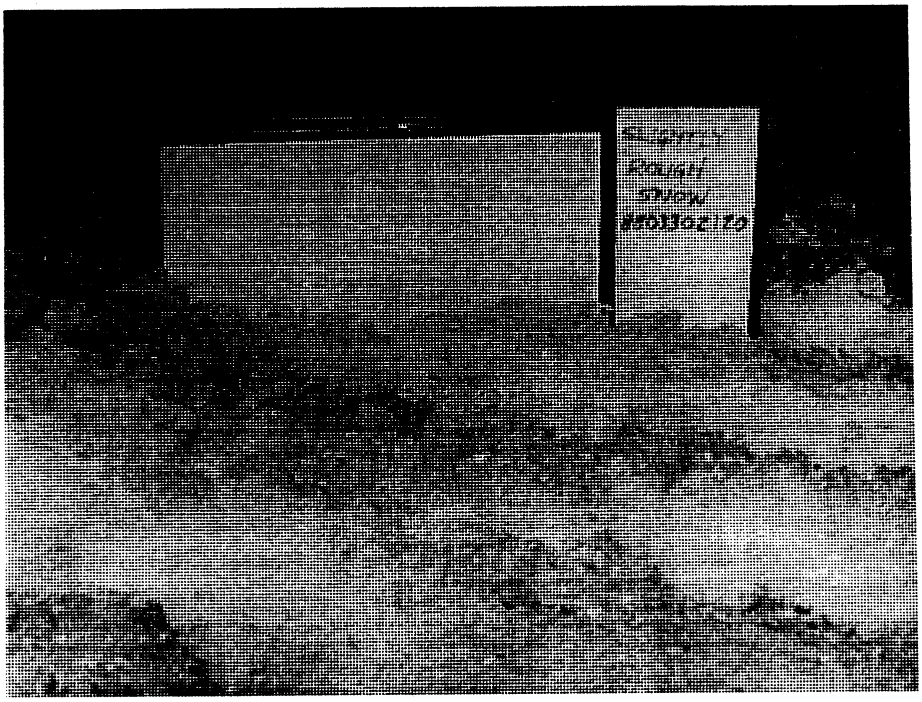

Figure 8: Cross sectional photograph of the "slightly rough" snow surface

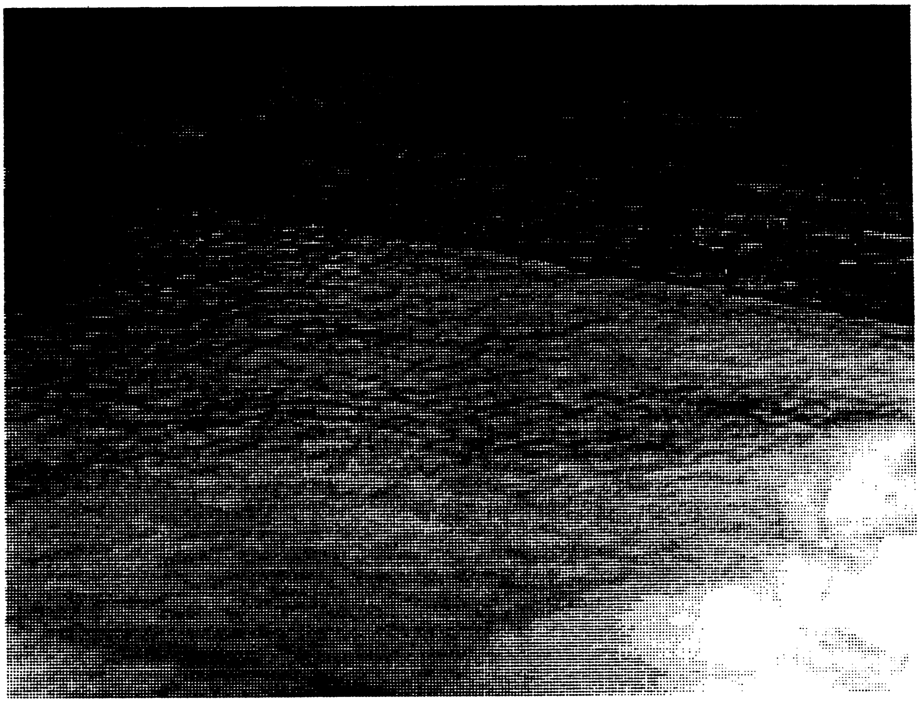

Figure 9: Undisturbed or "smooth" snow surface

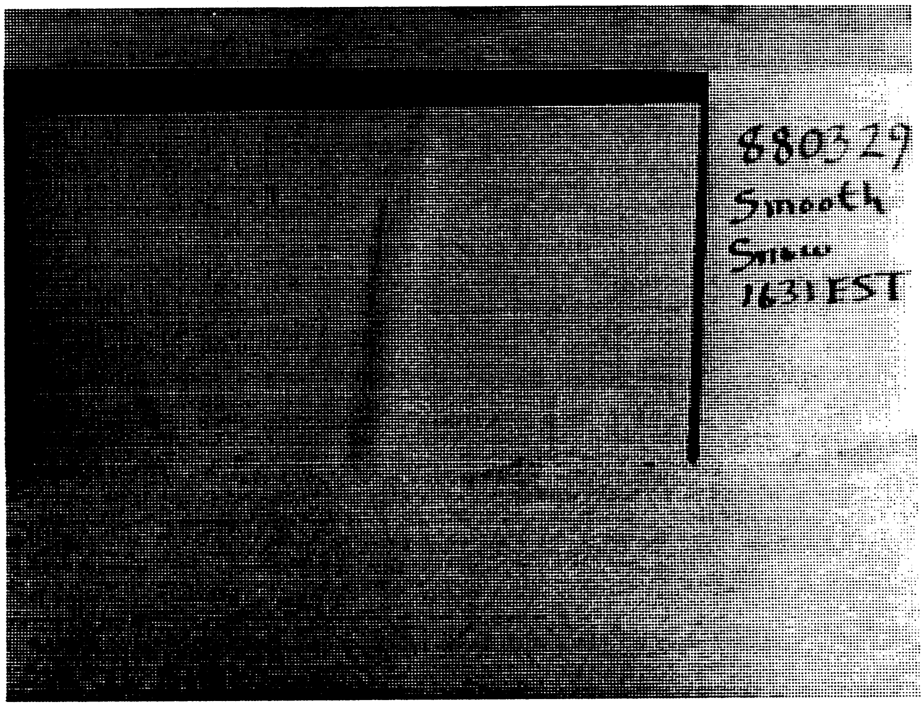

Figure 10: Cross sectional photograph of the undisturbed or "smooth" snow surface

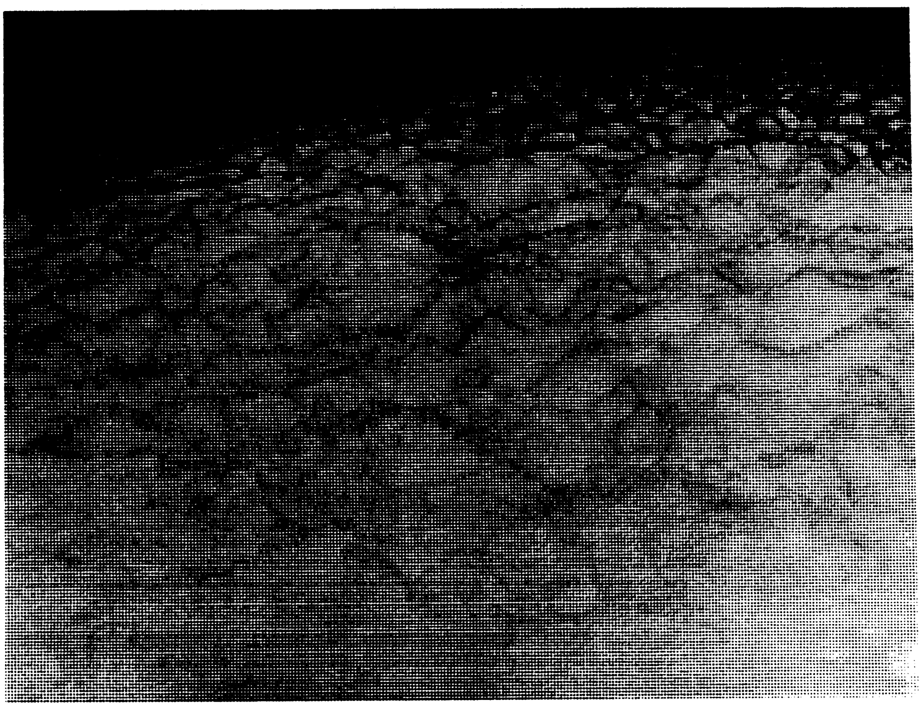

Figure 11: “Very rough” snow surface

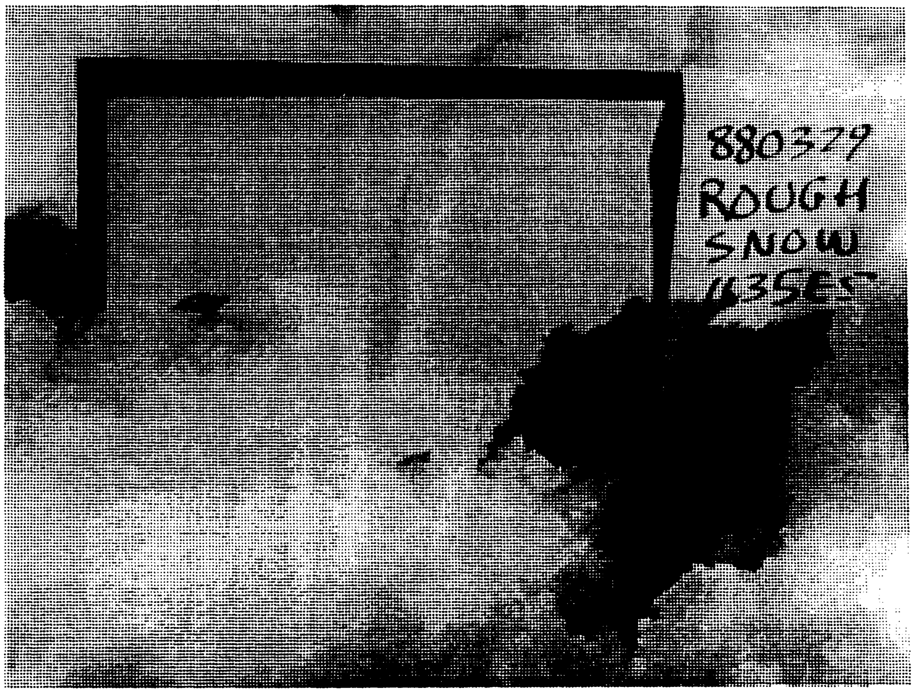

Figure 12: Cross sectional photograph of the "very rough" snow surface

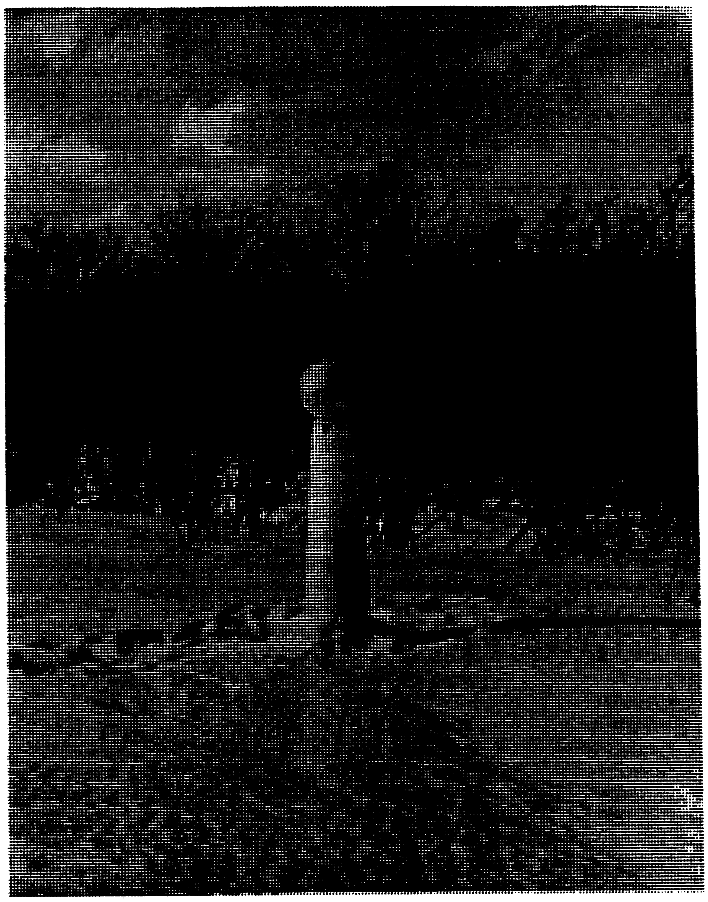

Figure 13: A 38.1 cm (15-inch) diameter aluminum sphere mounted atop a cylindrical styrofoam pedestal was used as a calibration target.

system was calibrated at regular intervals throughout the experiment.

3.2.3 Fading Variations

Fading-caused fluctuations in the backscatter measured from distributed targets are often overlooked. The topic of signal fluctuation statistics for distributed targets is treated in Ulaby *et al.* [3]. For a snow target, we assume that each target footprint contains a large number of independent scatterers, and that the

Figure 14: The boom was lowered to the illustrated position during calibration.

individual scatterers are comparable in magnitude; i.e., no single scatterer dominates the returned signal. Using these assumptions and others described in [3], we may assume that the backscattered signal follows a Rayleigh distribution (for square-law detection, which is our case). For such a distribution, the ratio of the standard deviation σ to the mean value μ of the backscatter is given by

$$\frac{\sigma}{\mu} = \frac{1}{\sqrt{N}} \tag{1}$$

where N is the number of independent samples, which can be obtained spatially (N_{sp}) and/or through frequency averaging (N_f).

In each target area, the radar was continuously swept in azimuth in order to increase N_{sp}. Approximately 40 independent samples per measurement were obtained by observing independent target areas.

Frequency averaging provided additional independent samples. For both 35 and 94 GHz measurements, a bandwidth of 2 GHz was used, providing more independent samples than a comparable single-frequency measurement.

As described in [3], the number of independent samples N_f obtained by frequency averaging is given by

$$N_f = \frac{2D}{c} B \tag{2}$$

where c is the velocity of light, B is the radar bandwidth (in hertz), and D is the difference in range (in meters) between the least and most distant points in the radar footprint. For our experiment, D was approximately 0.555 m and 0.164 m at 35 and 94 GHz, giving values of 7.41 and 2.19 for N_f at 35 and 94 GHz, respectively.

The total number of independent samples N is given by the product of N_f and N_{sp}. For our experiment, $N(35\text{GHz}) = 296$, and $N(94\text{GHz}) = 87.6$. Using (1), the expected values of σ/μ are 0.058 and 0.107, while our experimental values were 0.083 and 0.086 for 35 and 94 GHz, respectively.

3.2.4 Procedure

The experimental layout is shown in Figures 15 and 16. The three snow surfaces were measured in rotation at all frequencies and polarizations, in the following order: 35-vv, 35-hv[2], 94-vv, 94-vh, 94-hh. The incidence angle was 40° from nadir, and the average range to the snow surface was 9.34 m. During a given measurement run, the truck boom was swept in azimuth, moving the radar footprint back-and-forth within the boundaries of the surface area. A video camera and monitor allowed the operator to view the radar footprint during the measurement. At night, flashlights were placed at the boundaries of each surface area, allowing the operator to distinguish the boundaries when it was too dark to observe the snow directly on the monitor.

As a consequence of the limited area available for scanning, individual measurements of σ^0 were not completely spatially independent; i.e., the footprints (determined by the half-power beamwidth) did overlap. However, in Ulaby [3], we see that the returns from two footprints may be considered independent even if the footprints do overlap, provided that two conditions are satisfied: (1) $d > L_d$, where d is the distance between the centers of adjacent footprints and L_d, the *fading decorrelation distance,* is approximately $\ell_y/2$, where ℓ_y is the antenna width in the azimuth direction, and (2) $d > L_s$, where L_s is the spatial correlation length of the random surface. In the diurnal experiment, $d \geq 0.5$ m, $L_d = 7.62$ cm, and

---

[2] This report uses a *tr* convention for the cross-polarized backscattering coefficient; i.e., "vh" denotes transmit v, receive h.

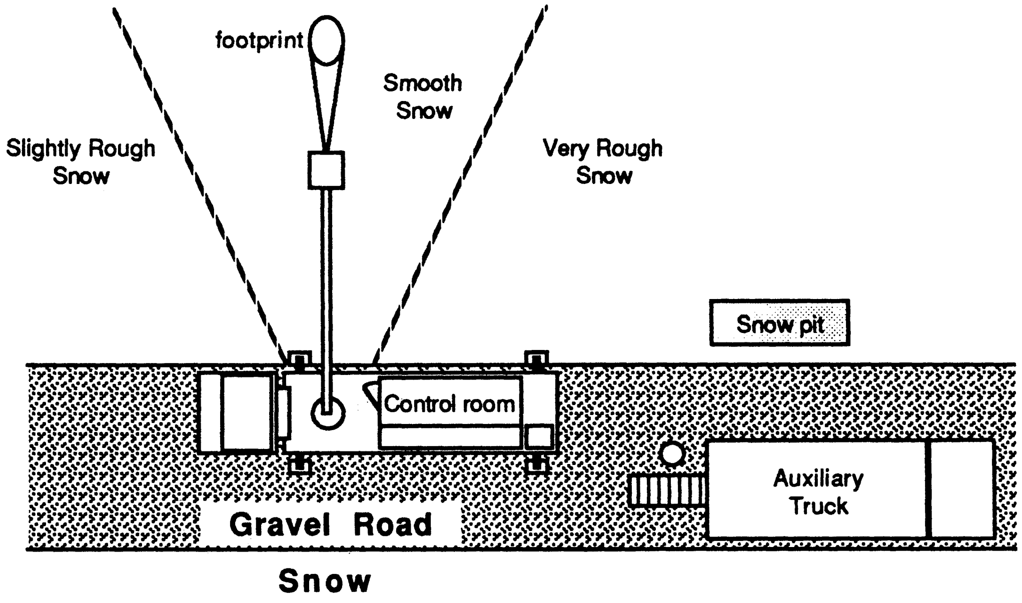

Figure 15: Top view of experiment site

$L_s < 0.5$ m for all three surfaces. Hence, the returns from all N_{sp} footprints were independent, giving N_{sp} independent samples (spatially).

4 Data Reduction

All data and supplementary information was recorded on a computer printout during the experiment. Upon returning to Ann Arbor, the data was entered into the university's mainframe computer for reduction.

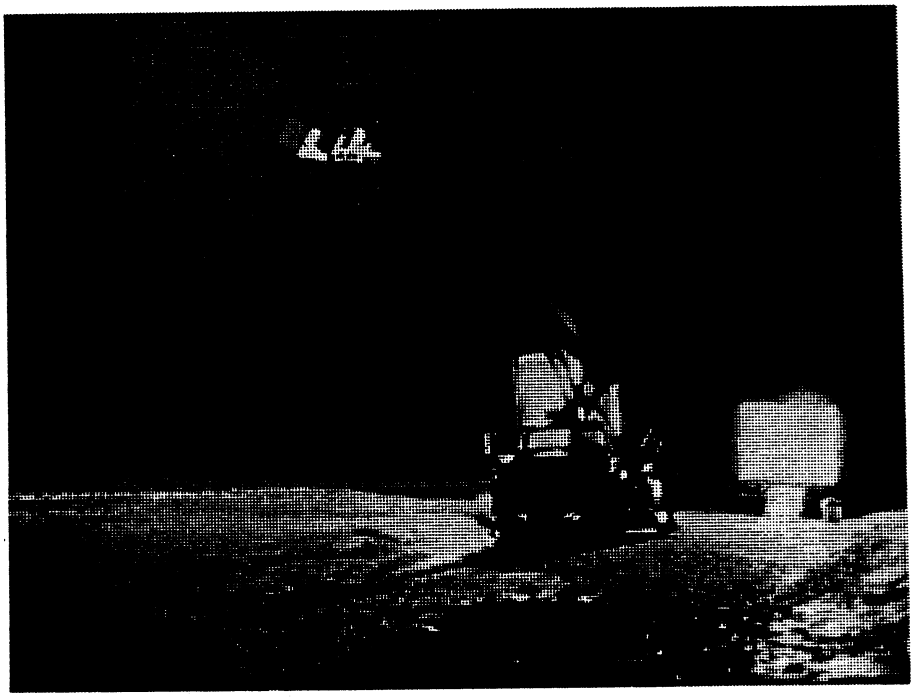

Figure 16: Nighttime view of experiment site

4.1 Calibration and Errors

The calibration target was a steel sphere with a diameter of 38.1 cm (15 inches). We begin with the point-target form of the radar equation:

$$P_r = \frac{P_t G_{t_p} G_{r_p} \lambda^2 \sigma_p}{(4\pi)^3 R_p^4} \tag{3}$$

where

P_r = received power

P_t = transmitted power

G_{t_p} = gain of transmit antenna in direction of sphere

G_{r_p} = gain of receive antenna in direction of sphere

λ = wavelength

σ_p = radar cross section of sphere

R_p = range of sphere from antennas

The calibration and measurements were performed using the time-domain option of the HP 8510, providing a real-time display of the ratio of received to transmitted power as a discrete function of range. The return signal from the sphere was clearly visible among the 401 trace points displayed on the screen of the HP 8510 (each corresponding to a particular range). The trace points representing the sphere return are summed to obtain the ratio of the total power reflected from the sphere to the power transmitted according to

$$P = \frac{P_r}{P_t} = \sum_{i=i_{\text{beg}}}^{i_{\text{end}}} \left(\frac{P_r}{P_t}\right)_i \tag{4}$$

Rewriting the radar equation, we now have

$$P = \frac{G_{t_p} G_{r_p} \lambda^2}{(4\pi)^3} \cdot \frac{\sigma_p}{R_p^4} \tag{5}$$

Let the terms on the left be represented by K:

$$K = \frac{G_{t_p} G_{r_p} \lambda^2}{(4\pi)^3} \tag{6}$$

Then

$$P = K \frac{\sigma_p}{R_p^4} \tag{7}$$

and, therefore,

$$K = \frac{R_p^4}{\sigma_p} P \tag{8}$$

which gives a value for K, the system constant. Note that this value is independent of range.

4.2 Illumination Integral and Generation of σ^0

To obtain values of the backscattering coefficient σ^0 we use the distributed-target form of the radar equation,

$$P_r = \frac{P_t \lambda^2}{(4\pi)^3} \int_{\text{Illuminated area}} G_t G_r \frac{\sigma^0}{R^4} \, dA \tag{9}$$

where

P_r = received power

P_t = transmitted power

λ = wavelength

G_t = gain of transmit antenna

G_r = gain of receive antenna

σ^0 = backscattering coefficient of distributed target

R = range of distributed target

Assuming σ^0 is constant over the pattern and using (4), we have

$$P = \frac{\lambda^2 \sigma^0}{(4\pi)^3} \int_{\text{Ill. area}} \frac{G_t G_r}{R^4} \, dA. \tag{10}$$

Let $G_t = G_{t0} g_t$ and $G_r = G_{r0} g_r$ where G_{t0} and G_{r0} are the maximum values of the transmit and receive antenna gains. We now have

$$P = \frac{\lambda^2 G_{t_0} G_{r_0} \sigma^0}{(4\pi)^3} \int_{\text{Ill. area}} \frac{g_r g_t}{R^4} \, dA \tag{11}$$

Assume G_{t_0} and G_{r_0} are the same as G_{t_p} and G_{r_p}. From (6), we have

$$P = K \sigma^0 \int_{\text{Ill. area}} \frac{g_r g_t}{R^4} \, dA \tag{12}$$

We define the integral in (12) as the *illumination integral I*. It is a function of the antenna patterns of the two antennas and the geometry of the measurement. Values of I were calculated for a wide range of antenna heights and incidence angles; interpolation of these results was used to obtain values for our measurements. Solving (12) for the backscattering coefficient, we have

$$\sigma^0 = \frac{P}{KI} \tag{13}$$

where I is the illumination integral, K is the system constant, and P is the ratio of the received to the transmitted power.

The value of K used for a particular measurement was that determined by the last preceding calibration. The assumption was that the system response was fairly constant over time.

5 Ground Truth

A variety of ground truth data were collected concurrently with the radar measurements. Ground truth data included air temperature, snow temperature profile, snow density, snow crystal characterization, snow surface profile, and snow gravimetric liquid water content. An excellent discussion of various ground-truth measurements of snow is found in Jones [4].

5.1 Snow Gravimeteric Liquid Water Content

5.1.1 Significance

The snow gravimetric liquid water content (GLWC) is perhaps the most important parameter that influences the radar backscatter. This is due to the large difference in the relative dielectric constants of liquid water ($\approx 10 - j20$ at 35 GHz) and ice (≈ 3.15). Thus, even a small amount of liquid water in a snowpack can cause a dramatic change in the backscatter characteristics of the snow.

5.1.2 Procedure

The snow gravimetric liquid water content was measured using a freezing calorimeter. This method has been determined to be the most accurate method for field measurements of GLWC [4,5], although the procedure is quite tedious and difficult to perform in the field.

A thermos containing a vacuum-sealed insulating bottle was modified for use as a calorimeter by drilling a small hole in the cap and inserting a thermistor (Omega Model ON-401-PP) through the cap. Toluene was used as the freezing agent. After several days of use, the plastic covering of the thermistor was dissolved by the toluene, rendering it unsafe. A Type K thermocouple was provided by the Keweenaw Research Center for use with the freezing calorimeter during most of the diurnal experiment.

The procedure is as follows: (1) The mass of the empty thermos is recorded. (2) Approximately 300 ml of toluene, which had been cooled to roughly -40 °C, is added to the thermos. (3) The mass of the thermos and toluene is recorded. (4) The thermos is closed with the thermistor inserted in the toluene. (5) While agitating the calorimeter gently, the temperature of the toluene is recorded at 15-second intervals. When the rate of temperature change is roughly constant (usually within about 5 minutes), the thermos is considered to be at equilibrium, with a small amount of heat leaking into the thermos at a constant rate. (6) The snow sample is collected, its temperature is noted, and it is added to the toluene in the thermos. (7) The exact time that the snow is added is recorded, and the agitation and 15-second interval temperature recordings are resumed. The temperature is monitored until the rate of temperature change is again constant. At this point, the liquid water in the snow sample has been frozen and the mixture is again in equilibrium, except for the small leakage into the calorimeter. (8) The mass of the thermos, toluene, and snow sample is recorded. (9) The toluene/snow mixture is then discarded, and the thermos is cleaned in preparation for the next

Figure 17: A sample is collected from the surface of the snow for the gravimetric liquid water content measurement.

measurement. An entire measurement sequence, including cleanup, took 30–40 minutes when performed by a single operator. Various steps in the procedure are illustrated in Figures 17, 18, and 19.

Through later experience we learned the importance of vigorous agitation of the calorimeter during the temperature measurements. The gentle agitation recommended in earlier reports [4,5] and used in this experiment may have contributed to experimental errors. We recommend vigorous agitation and inversion of the calorimeter in order to obtain adequate mixing and accurate temperature measurements.

The fraction of the snow mass which is in the liquid state is determined by one

Figure 18: The calorimeter is gently agitated and the temperature is recorded every 15 seconds.

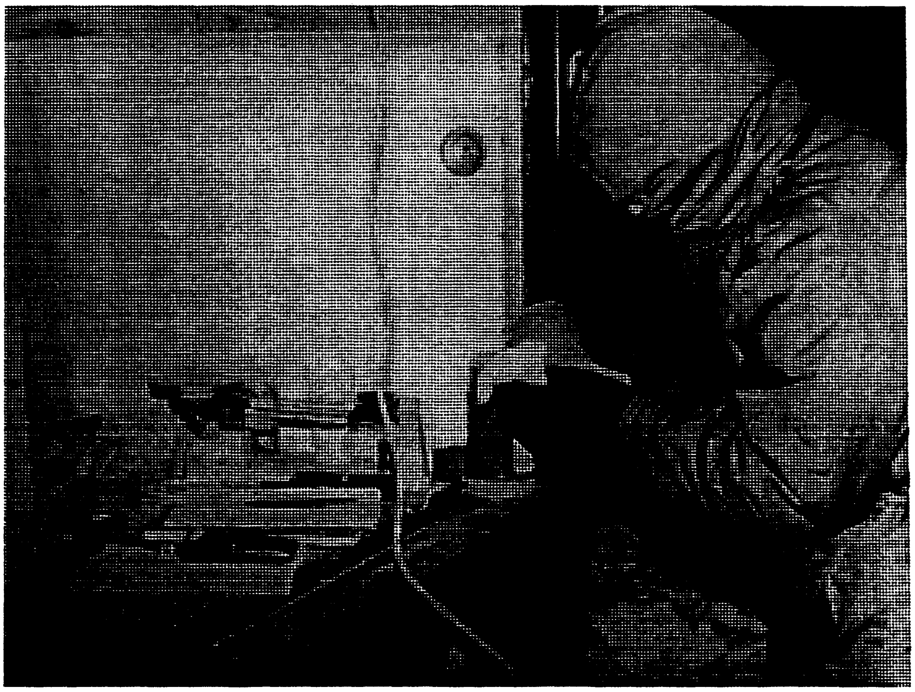

Figure 19: The calorimeter must be thoroughly cleaned after each measurement.

of the following two equations. If the snow temperature is greater than the freezing point of water ($T_s \geq T_z$), we have

$$\frac{m_w}{m_s} = \frac{(m_T + E)C_{Tif}(T_f - T_i) - m_s C_{dzf}(T_z - T_f)}{m_s[L + C_{wsz}(T_s - T_z)]} \tag{14}$$

If the snow temperature is less than the freezing point of water ($T_s \leq T_z$), we have

$$\frac{m_w}{m_s} = \frac{(m_T + E)C_{Tif}(T_f - T_i) - m_s C_{dsf}(T_s - T_f)}{m_s[L - C_{dsf}(T_s - T_f) + C_{dzf}(T_z - T_f)]} \tag{15}$$

where

m_w = mass of liquid water in the snow (g)

m_s = mass of snow (including both liquid and solid components) (g)

m_T = mass of the toluene (g)

E = calorimeter constant (g)

T_f = final temperature of the toluene/snow mixture (K)

T_i = temperature of the toluene before adding the snow sample (K)

T_z = freezing point of water (= 273.15 K)

T_s = temperature of the snow sample prior to adding to the toluene

L = heat of fusion of water (= 79.7 cal/g)

C_{Tif} = heat capacity of toluene at $T = (T_i + T_f)/2$ (cal/g $\cdot$ K)

C_{dzf} = heat capacity of ice at $T = (T_z + T_f)/2$ (cal/g $\cdot$ K)

C_{wsz} = heat capacity of water at $T = (T_s + T_z)/2$ (cal/g $\cdot$ K)

C_{dsf} = heat capacity of ice at $T = (T_s + T_f)/2$ (cal/g $\cdot$ K)

The results of the liquid water measurements are shown in Figure 20, where

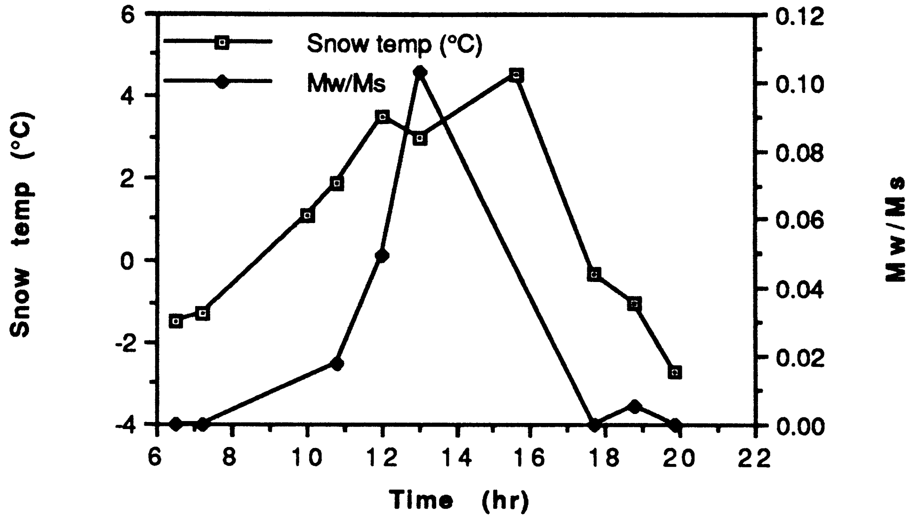

Figure 20: Measured gravimetric liquid water content of the snow

gravimetric liquid water content is plotted along with T_s, the snow temperature near the surface.

5.2 Snow Pit Data

Most of the other ground truth parameters were measured in the snow pit by various members of the experiment team. The snow pit was dug in an area adjacent to the radar target area, as shown in Figure 15. The snow pit is illustrated in Figures 21 and 22. Care was taken not to disturb the front face of the pit, which was used to characterize the snow at varying depths. Periodically, the pit was extended in the direction of the front face, thus exposing a fresh profile which had been unexposed to air and/or sun. The front face of pit was exposed on the north side; hence it was shaded at all times.

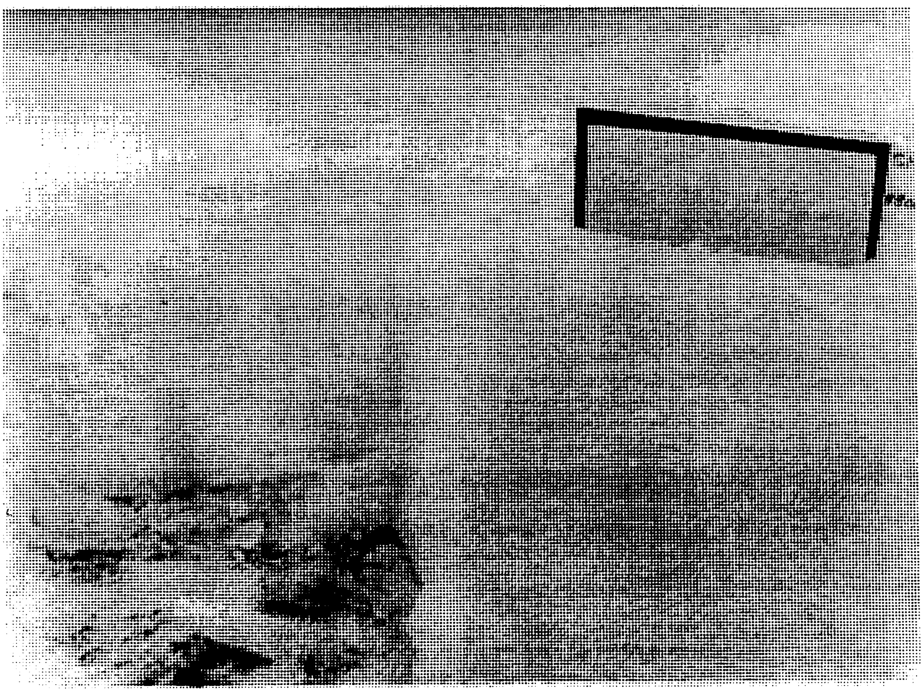

Figure 21: The face of the snow pit

Figure 22: A technician collects a density sample from the snow pit.

Surface	rms roughness	Std. Dev.
smooth	0.488 cm	0.161 cm
slightly rough	0.880 cm	0.314 cm
very rough	1.976 cm	1.130 cm

Table 1: Mean and standard deviation of rms roughness of various surface areas

5.2.1 Surface Profile

Snow surface profiles were used to estimate the roughness of the snow surface. In each surface area, a flat plate was inserted vertically into the snowpack and the snow on one side was removed, exposing a cross section of the snow surface. The profile of the surface was then photographed with a ruled grid placed in the background for comparison. The resulting surface profiles are shown in Figures 8, 10, and 12. The surface roughnesses are summarized in Table 1.

5.2.2 Snow Temperature

A snow temperature profile was obtained by inserting mercury thermometers into the face of the snow pit at varying depths. In addition, a thermometer was inserted almost horizontally into the upper centimeter of the snowpack, giving regular "surface snow" readings. The snow temperatures are summarized in Table 2.

5.2.3 Air Temperature

Air temperature was monitored by an alcohol thermometer which was suspended in air in the shade (under the equipment truck, which remained stationary with its engine off throughout the entire experiment). Air temperatures are sum-

Time (hr)	Snow temperature (°C)	Air temperature (°C)
6.5	-1.5°	-1.8°
7.23	-1.3°	-2.0°
10.05	1.1°	-1.0°
10.8	1.9°	-0.5°
12.03	3.5°	0.5°
13.03	3.0°	0.8°
15.58	4.5°	1.1°
17.7	-0.3°	0.0 °
18.78	-1.0°	-1.5°
19.87	-2.7°	-1.5°

Table 2: Snow and air temperatures during diurnal experiment

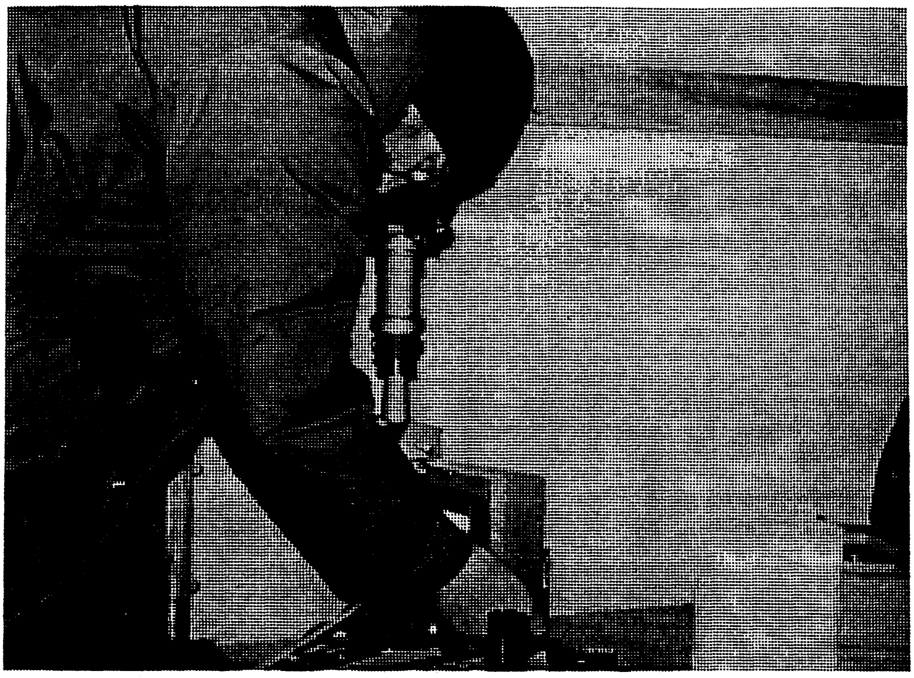

Figure 23: Snow crystals were photographed using a microscope with 35 mm camera attachment.

marized in Table 2.

5.2.4 Snow Crystal Characterization

Snow crystal type was recorded using a microscope with a 35 mm camera attachment (Figure 23). As shown in Figure 4, the upper snow surface did not contain many intact snow crystals. The heavily metamorphosed snow was mostly in the form of icy clumps, with occasional abrasions showing.

There was a brief period of snowfall on the morning of the experiment, although there was no significant accumulation. Figure 24 shows the fresh snow against a footprint in mud that had been free of snow before the brief snowfall. A sample of the freshly fallen snow crystals is shown in Figure 25.

Figure 24: The brief period of snowfall on the morning of the experiment resulted in negligible accumulation.

There was a brief period of snowfall on the morning of the experiment, although there was no significant accumulation. Figure 24 shows the fresh snow against a footprint in mud that had been free of snow before the brief snowfall. A sample of the freshly fallen snow crystals is shown in Figure 25.

6 Discussion

In spite of the limited scope of this experiment, the surface preparation and ground truth data allow us to analyze the effects of several variables on the radar backscatter.

Figure 25: Freshly fallen snow crystals

6 Discussion

In spite of the limited scope of this experiment, the surface preparation and ground truth data allow us to analyze the effects of several variables on the radar backscatter.

6.1 Diurnal Variations

The diurnal experiment began at 6:37 AM local time on March 31 and concluded at 9:57 PM. Starting before sunrise and ending well after sunset allowed the observation of a complete melt/freeze cycle. A graph of the backscattering coefficient vs. time is shown in Figure 26, which includes data for all five frequency/polarization combinations for the undisturbed or "smooth" snow. Actual data points are shown along with curve fits using Gaussian curves with constant offsets. As expected, backscatter is higher for the cooler periods before sunrise and after sunset. Temperatures during these periods were several degrees below the freezing point of water, resulting in completely dry snow, composed only of ice particles. During the day, the warm temperatures melted some of the surface snow, resulting in decreased backscatter due to the large increase in dielectric constant as ice changes to liquid water.

Figure 26 also shows the dependence of σ^0 on frequency and polarization. The backscattering coefficient is higher at 94 GHz than at 35 GHz due to the increased roughness of the surface compared to a wavelength. The like-polarized return is dominant over the cross-polarized return at both frequencies, as expected.

Similar graphs for the slightly rough and very rough cases are shown in Fig-

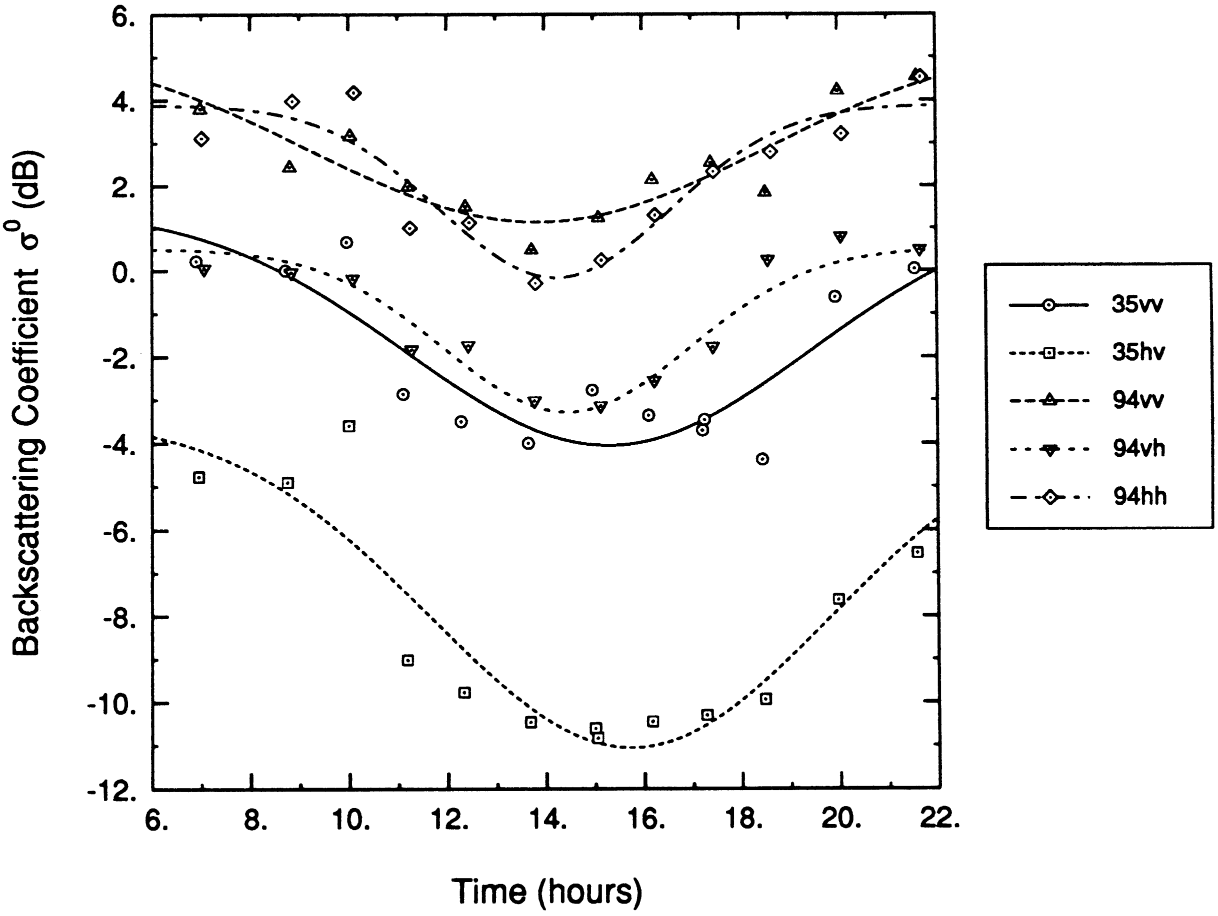

Figure 26: Backscatter from undisturbed snow surface as a function of time. Symbols are actual data points. Lines are best fits to the data.

ures 31 and 32 in the Appendix.

6.2 Surface Variations

The snow target area was divided into three areas to observe the effect of surface roughness. The backscattering coefficients for all three areas are shown in Figure 27 for 35 GHz, vv-polarization, and in Figure 28 for 35 GHz, hv-polarization.

As described previously, the undisturbed section was quite smooth, having been blown smooth by the wind. As expected, this surface type had the smallest values of σ^0 at 35 GHz for both like- and cross-polarized returns. Returns from slightly rough and very rough surfaces were mostly 0.5-1.5 dB higher for vv, and 0.7-2.4 dB higher for hv, indicating that the rough snow depolarizes more than the smooth snow.

Backscatter at 94 GHz seems less dependent on surface roughness, with smooth, slightly rough, and very rough returns all within 2 dB and often within 1 dB of each other. This is presumably because all three of the surfaces were "rough" compared to the wavelength at 94 GHz (λ = 3.2 mm). Indeed, the rms surface roughnesses for the three surfaces are 1.525λ, 2.750λ, and 6.175λ at 94 GHz.

Graphs of σ^0 vs. time for the three surfaces at 94 GHz are shown in Figures 33, 34, and 35 in the Appendix.

6.3 Variation of Backscattering Coefficient with Liquid Water Content

Since gravimetric liquid water content (GLWC) seems to be the dominant factor in determining the backscattering coefficient, it was desired to observe this relationship directly. In order to accomplish this, it was first necessary to charac-

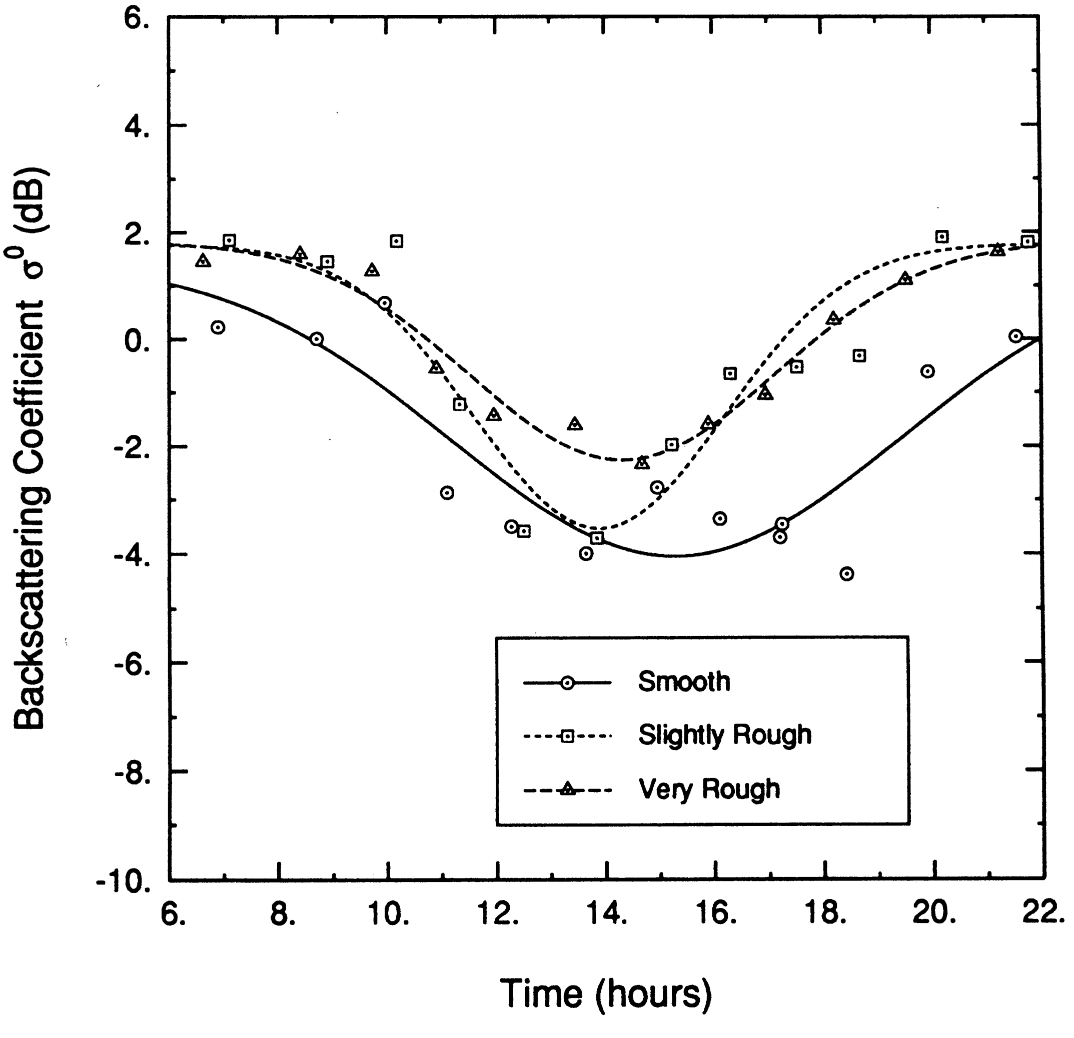

Figure 27: Backscatter from three snow surfaces as a function of time at 35 GHz, vv-polarization.

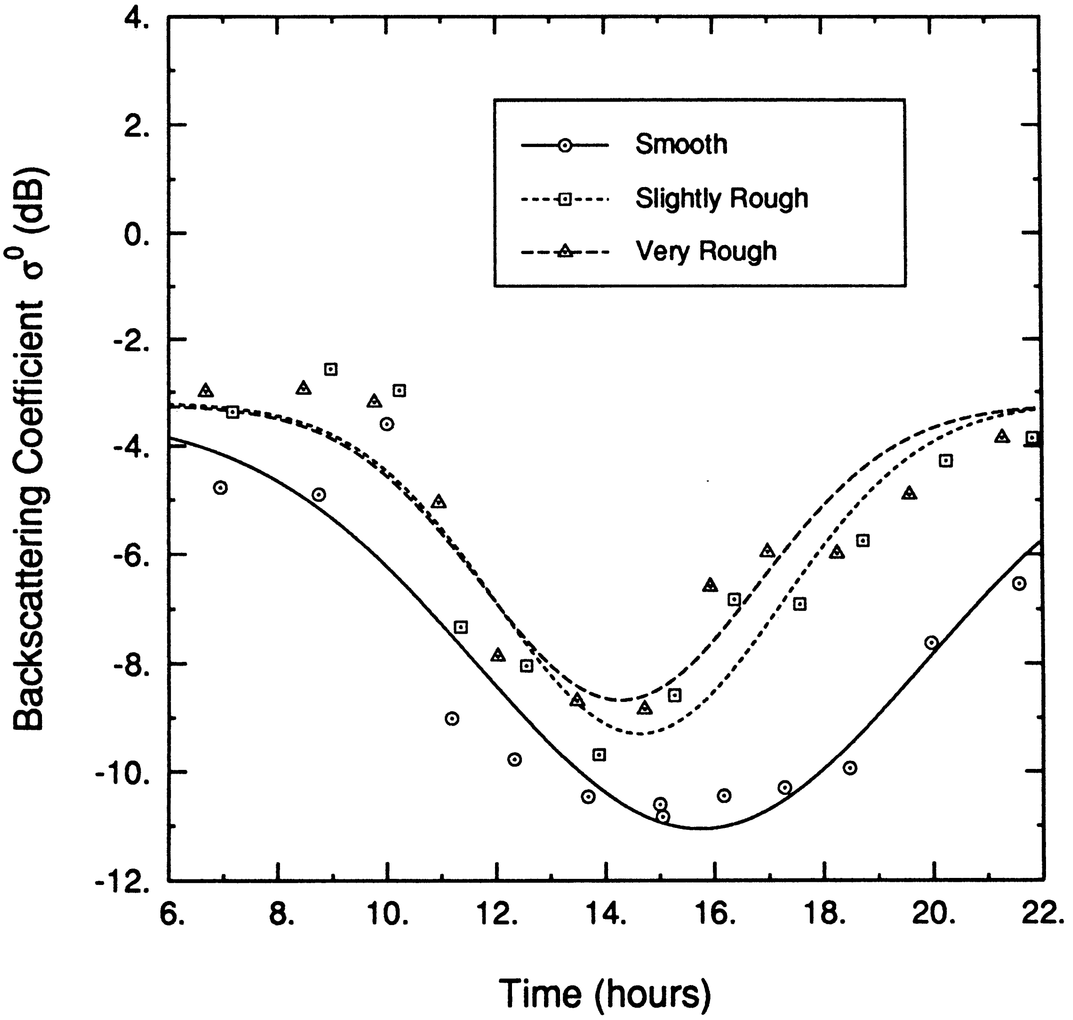

Figure 28: Backscatter from three snow surfaces as a function of time at 35 GHz, hv-polarization.

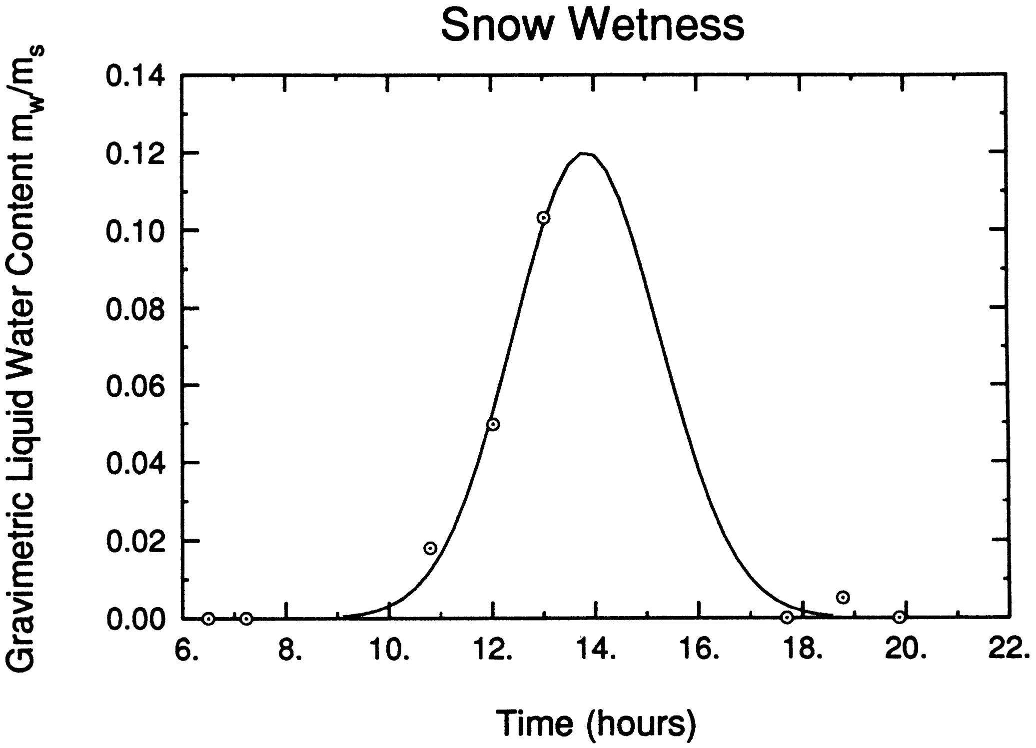

Figure 29: Functional fit to measured gravimetric liquid water content of the snow

terize the variation of GLWC with time, since the liquid water measurements were not simultaneous with the radar measurements. A Gaussian curve with constant offset was fit to the liquid water data points to provide a usable (though obviously imperfect) approximation to the variation in GLWC. This approximation and the actual data points are shown in Figure 29.

Next, values of σ^0 were plotted against estimated snow GLWC at the time of each radar measurement. The results were somewhat mixed. Although there is a clear decrease in σ^0 with increasing GLWC, the scatter in some of the data sets, especially for the dry snow, leads us to believe that a few of the data points may

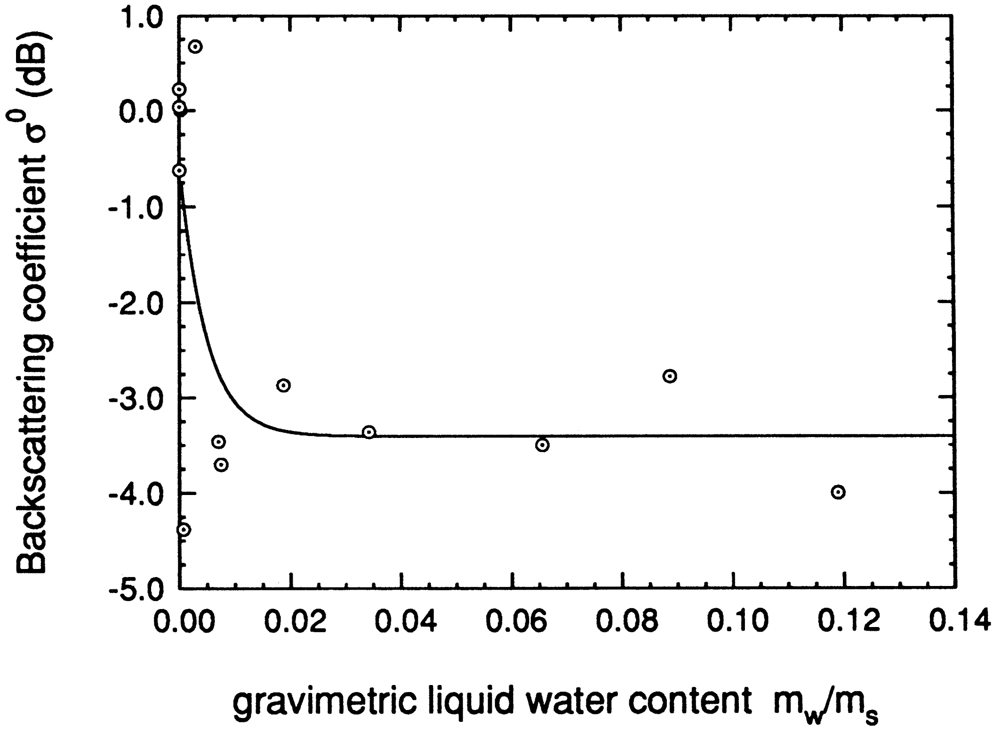

Figure 30: Backscattering coefficient as a function of gravimetric liquid water content for undisturbed snow at 35 GHz, vv-polarization.

be questionable. However, most of the data do seem to follow expected trends, at least qualitatively. A much larger collection of data is needed to reduce the fraction of outlying points. In addition, an increase in ground truth data quality and quantity is needed so that other variables may be considered.

Since we expect σ^0 to decrease rapidly with small values of GLWC and then level out somewhat, an exponential function with constant offset was fit to measured data for all fifteen combinations of frequency, polarization, and surface type. The 35 GHz, vv-polarized, smooth surface case is shown in Figure 30. The form of the equation was

$$\sigma^0_{fit} = A + B\exp(-Cx) \tag{16}$$

where $x = m_w/m_s$, and A, B, and C are arbitrary constants chosen to minimize the χ^2 error, where

$$\chi^2 = \sum_{i=1}^{N}(\sigma^0_i - \sigma^0_{fit})^2 \tag{17}$$

The coefficients A, B, and C are given in Table 3, along with the corresponding values of χ^2. The remainder of the plots of the fitted curves and data points are shown in Figures 36-49 in the Appendix.

7 Recommendations for Future Snow Experiments

The diurnal experiment described in this report was one of the first operational uses of the MMP system in a non-laboratory setting and the first full-scale snow experiment performed by the research team. In the long run, the experience gained in performing this experiment will probably outweigh the data that was collected.

This section is meant to serve as a guide to those who will be participating in the more extensive snow experiments planned for the winter of 1988-89.

7.1 Data Collection

The most obvious recommendation for future experiments is that the quantity of data taken should rise dramatically. Measurement hardware and software should be optimized to increase data rates and facilitate simple operation by the equipment operator. Snow data should be collected on a wide variety of snow types and

Freq.	Pol.	Surface	A	B	C	χ^2
35 GHz	vv	sm	-3.407104	2.860178	207.6808	21.96233
		sr	-4.030170	5.319317	20.37669	7.871177
		vr	-1.769970	3.129681	90.59702	1.624946
	hv	sm	-10.44650	4.089747	77.99965	37.64211
		sr	-9.170826	5.131781	32.54294	15.09465
		vr	-9.239279	5.271280	21.75925	8.898164
94 GHz	vv	sm	0.6074919	2.691298	21.86616	5.975779
		sr	1.261313	2.358287	11.91724	7.661778
		vr	1.007773	1.989005	46.85294	2.489407
	vh	sm	-2.494925	2.899044	180.8764	3.088548
		sr	-2.069181	2.596421	77.20051	5.467927
		vr	-2.051307	2.357536	137.0364	2.490696
	hh	sm	0.2231809	3.389608	44.24685	4.701183
		sr	-0.2360335	4.196653	12.82903	8.415516
		vr	1.266275	2.586488	161.4549	7.175722

Table 3: Coefficients of curve fit to liquid water data

surface roughnesses, which may be natural or man-made. Time and temperature variations are also of interest.

An extensive preparation period will help insure that all experiments proceed smoothly. Radar and radiometer hardware should be hardened to withstand expected extremes in temperature as well as the other hazards of vibration, power variation, dust, etc. which always accompany experiments in the field. Extensive testing and debugging of all measurement software should avoid many computer problems in the field. Practice measurement sessions will aid in the early detection of potential problems.

Since it is obviously impossible to measure snow backscatter and emission as a function of *all* variables (due to the limited resources of time, personnel, and snow), careful thought needs to be given to select a set of variables which will maximize the return on resources devoted to the snow experiment. Specific theoretical questions need to be selected early in order to avoid unnecessary measurements.

7.2 Ground Truth

The increase in the quantity of backscatter and emission data must be accompanied by a corresponding or even more extensive increase in ground truth data. The collection of ground truth data *must* be regarded as a primary task which is every bit as important as (and often much more difficult than) the collection of radar/radiometer data.

Ground truth equipment and procedures should be improved to increase the sampling rate as much as possible. In each experiment, several people should have the responsibility of collecting ground truth data only. These individuals should be thoroughly trained and allowed to practice ground truth techniques before the actual experiment. Standard forms should be created to facilitate the recording and processing of ground truth data. Extensive photographs of the experiment site are necessary for later analysis of experimental data.

The determination of the snow liquid water content is the most difficult yet most vital ground truth procedure. A better insulated calorimeter with a more durable temperature probe would increase the accuracy of the GLWC measurements. An alternate freezing agent, such as silicone oil, would be preferable to toluene due to the toxicity and low flash point of toluene. An electronic scale, capable of withstanding cold temperatures, would speed the measurement process. Dry ice should be investigated as a means to cool the freezing agent, rather than the liquid nitrogen which was used in this experiment. Leaving the freezing agent/snow mixture in the calorimeter until just before the next measurement helps keep the calorimeter cool, resulting in shorter times necessary to reach equilibrium.

It is especially important that GLWC data be taken often throughout the experiment; this will give a detailed picture of the snow GLWC with time and will reduce the effect of any bad data points. Printed forms for GLWC data or, even better, computerized recording of this data will help speed the process. Two people should be assigned to collect GLWC data alone—perhaps running two calorimeters in rotation.

7.3 Miscellaneous Items

Some miscellaneous items that were quite useful or that would have been useful include a snow shovel, several extra thermometers, several containers for snowgathering, salt or sand for the work area, and a 40-liter container of water for drinking, washing, cleaning, etc. A separate generator is recommended for the mobile lab to allow more flexibility in location and to decrease the load on the truck generator.

References

[1] NASA Snowpack Properties Working Group, *Plan of Research for Snowpack Properties Remote Sensing - (PRS)^2*, Goddard Space Flight Center, June 1982.

[2] Ulaby, F. T., T. F. Haddock, J. East, and M. Whitt, "A Millimeter-Wave Network Analyzer Based Scatterometer," *IEEE Transactions on Geoscience and Remote Sensing*, vol. GE-26, no. 1, January 1988, pp. 75–81.

[3] Ulaby, F. T., T. F. Haddock, and R. T. Austin, "Fluctuation Statistics of Millimeter-Wave Scattering From Distributed Targets," *IEEE Transactions on Geoscience and Remote Sensing*, vol. GE-26, no. 3, May 1988, pp. 268-281.

[4] Jones, E. B., *Snowpack Ground-Truth Manual*, NASA Contractor Report 170584, May 1983.

[5] Stiles, W. H., and F. T. Ulaby, *Microwave Remote Sensing of Snowpacks*, NASA Contractor Report 3263, June 1980.

[6] Stiles, William H., and Fawwaz T. Ulaby, "The Active and Passive Microwave Response to Snow Parameters: 1. Wetness," *Journal of Geophysical Research*, vol. 85, no. C2, February 20, 1980, pp. 1037-1044.

[7] Ulaby, Fawwaz T., and William H. Stiles, "The Active and Passive Microwave Response to Snow Parameters: 2. Water Equivalent of Dry Snow," *Journal of Geophysical Research*, vol. 85, no. C2, February 20, 1980, pp. 1045-1049.

[8] Williams, Larry D., John G. Gallagher, David E. Sugden, and Richard V. Birnie, “Surface Snow Properties Effects on Millimeter-Wave Backscatter,” *IEEE Transactions on Geoscience and Remote Sensing*, vol. GE-26, no. 3, May 1988, pp. 300-306.

[9] Williams, Larry D., and John G. Gallagher, “The Relation of Millimeter-Wavelength Backscatter to Surface Snow Properties,” *IEEE Transactions on Geoscience and Remote Sensing*, vol. GE-25, no. 2, March 1987, pp. 188-194.

[10] Williams, L. D., R. V. Birnie, and J. G. Gallagher, “Millimeter-Wave Backscatter from Snowcover,” *Proceedings of the 1985 International Geoscience and Remote Sensing Symposium, Amherst, Mass.*, pp. 842-847.

Appendix

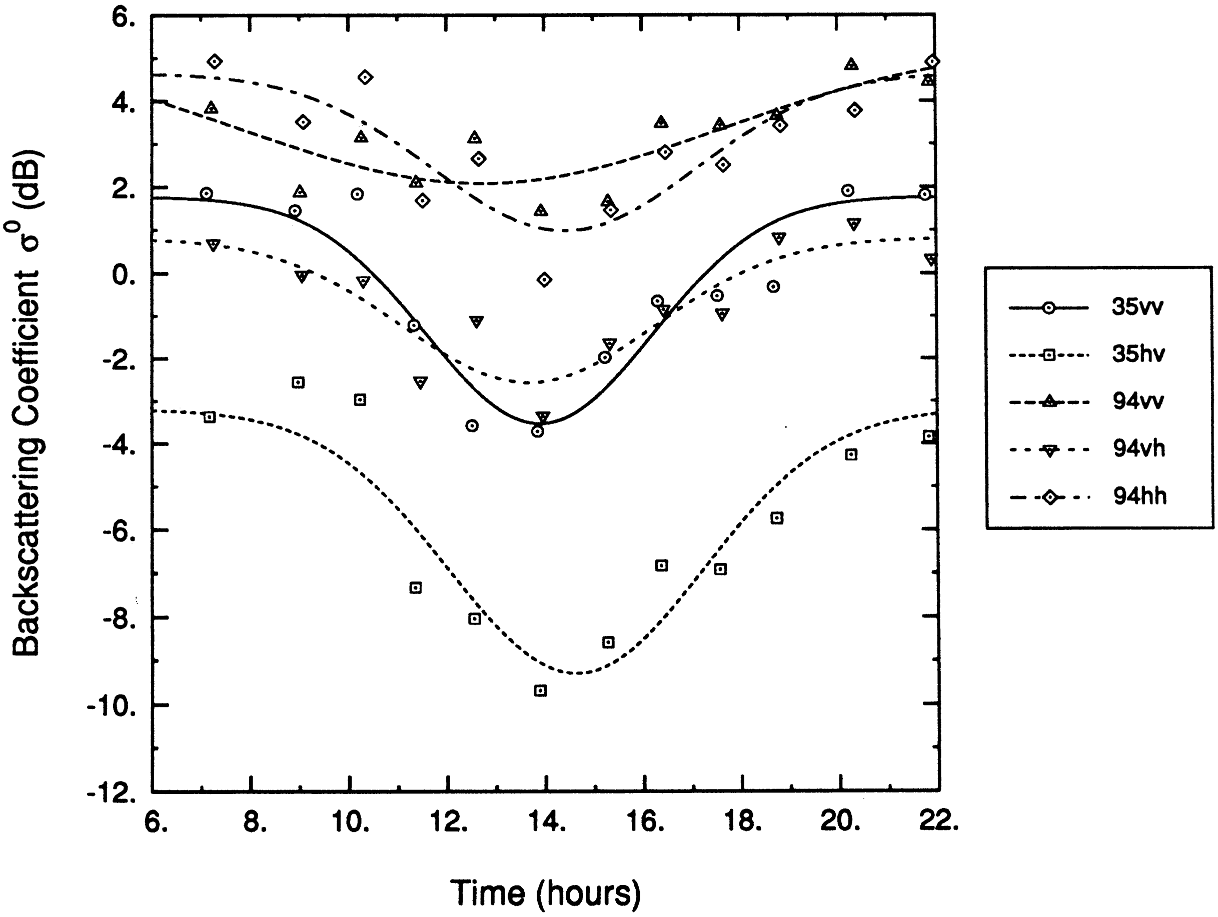

Figure 31: Backscatter from slightly rough snow surface as a function of time.

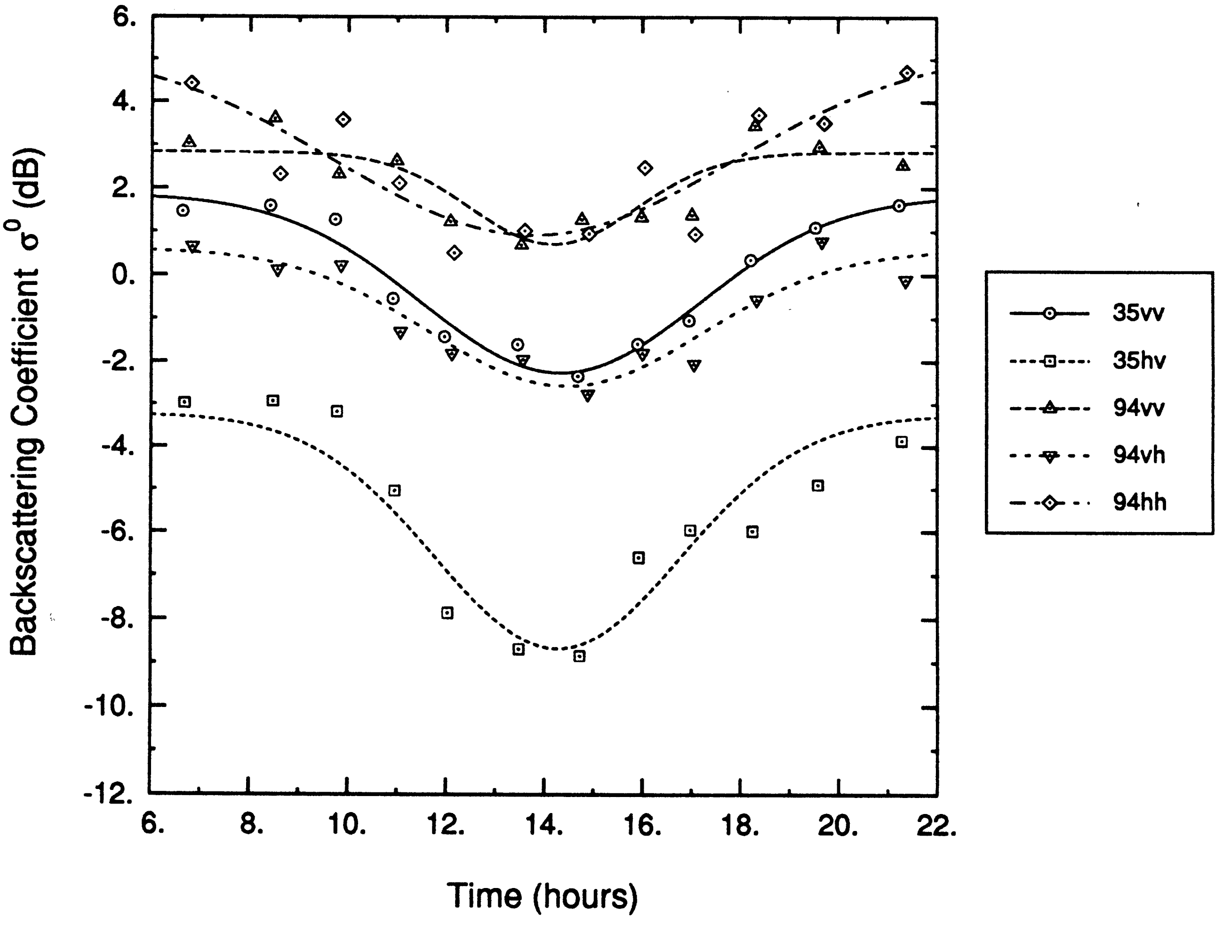

Figure 32: Backscatter from very rough snow surface as a function of time

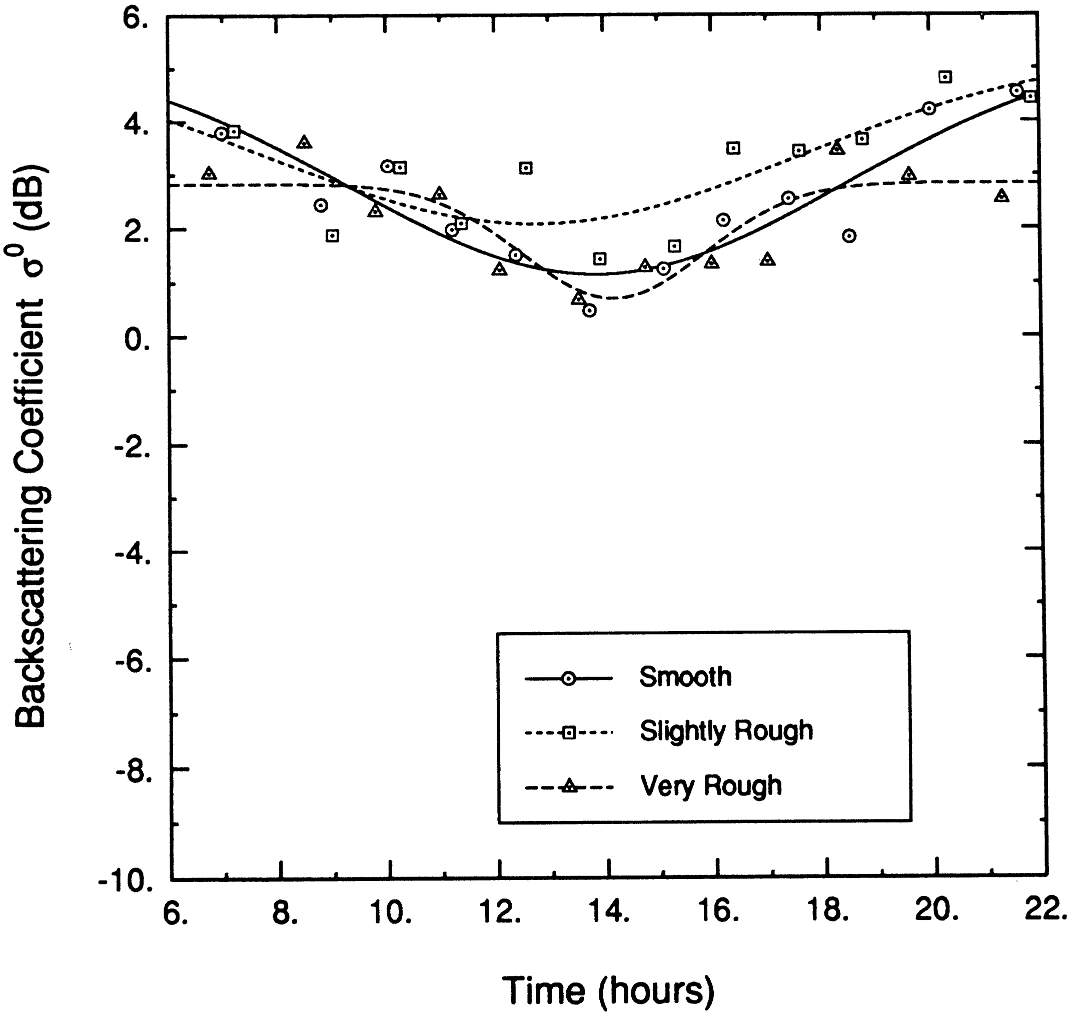

Figure 33: Backscatter from three snow surfaces as a function of time at 94 GHz, vv-polarization

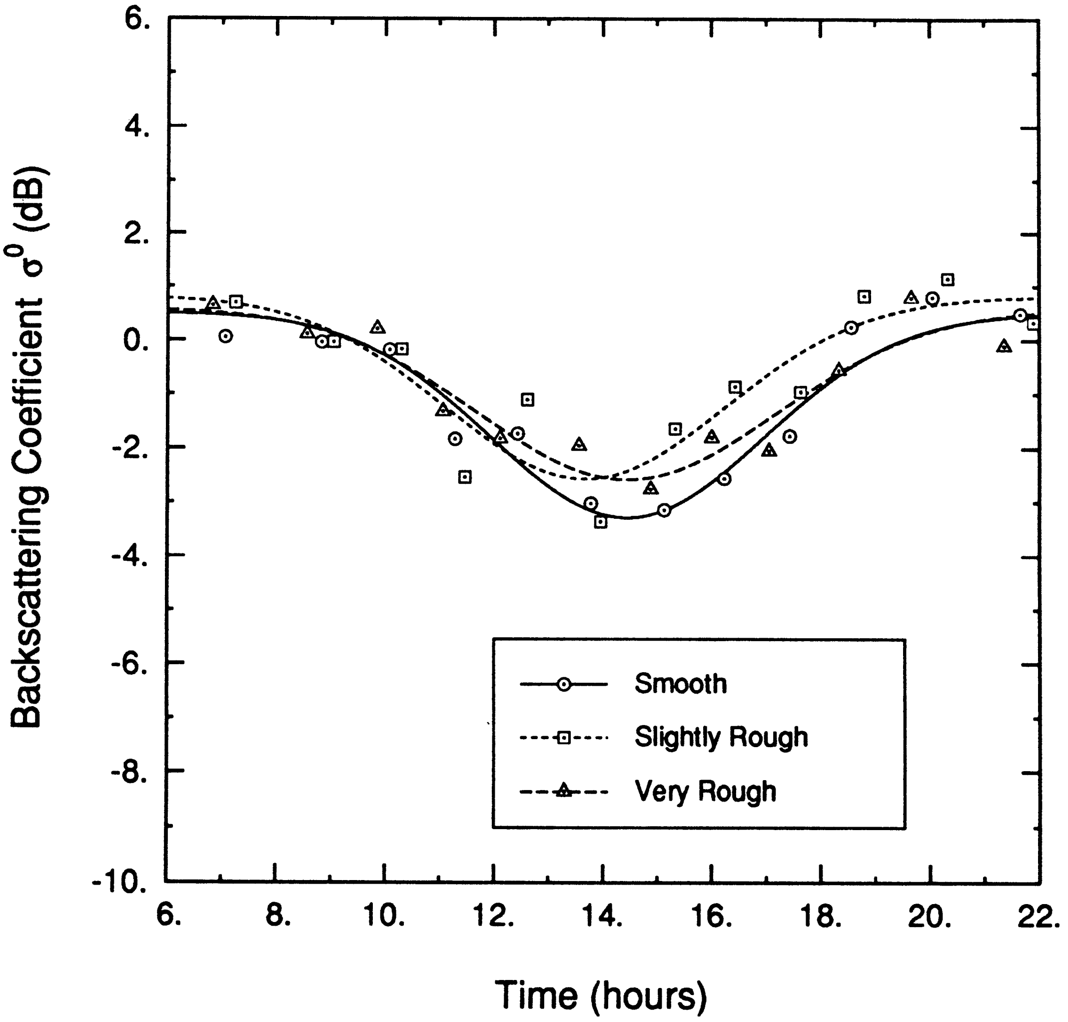

Figure 34: Backscatter from three snow surfaces as a function of time at 94 GHz, vh-polarization

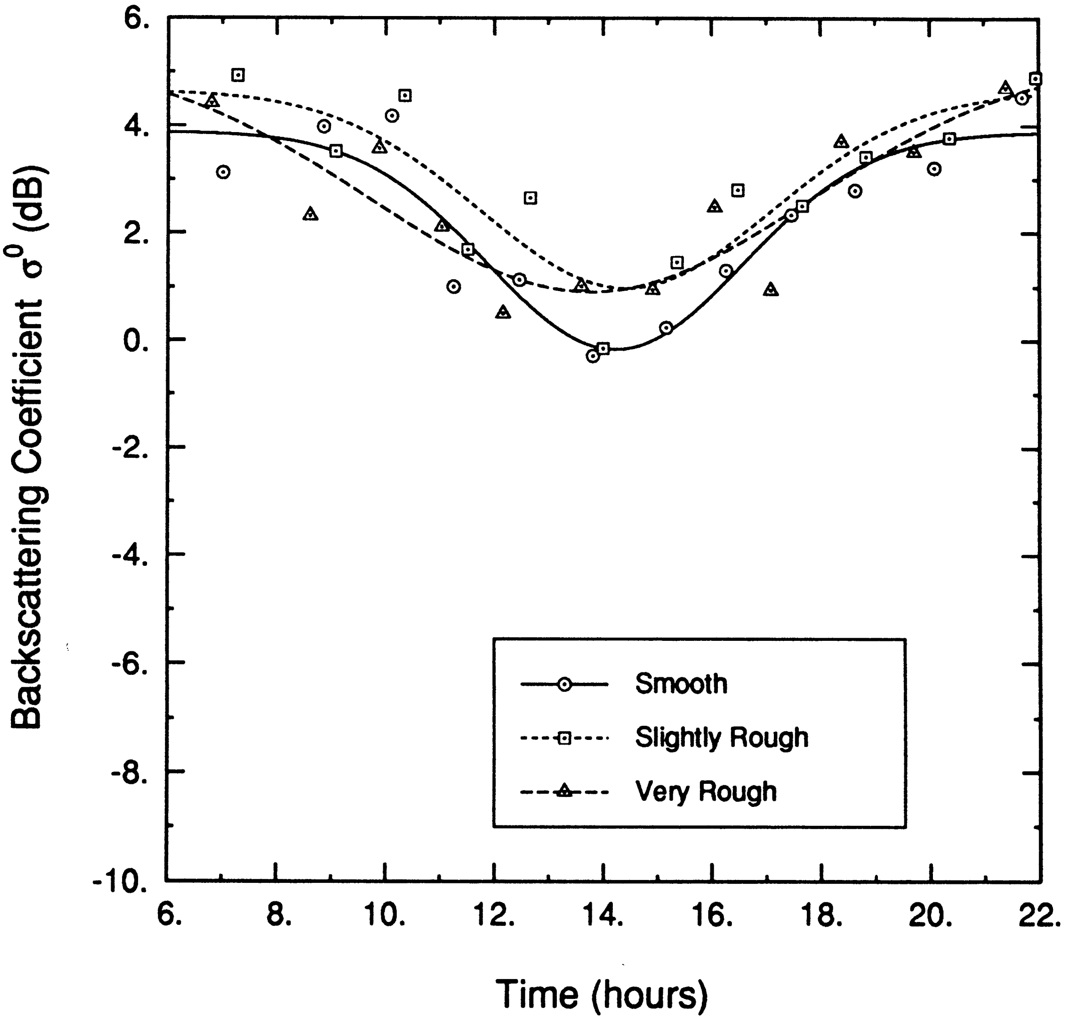

Figure 35: Backscatter from three snow surfaces as a function of time at 94 GHz, hh-polarization

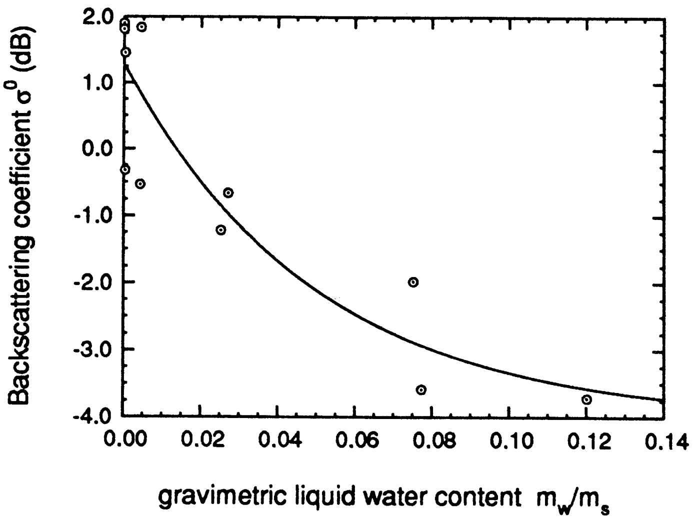

Figure 36: Backscattering coefficient as a function of gravimetric liquid water content for slightly rough snow at 35 GHz, vv-polarization

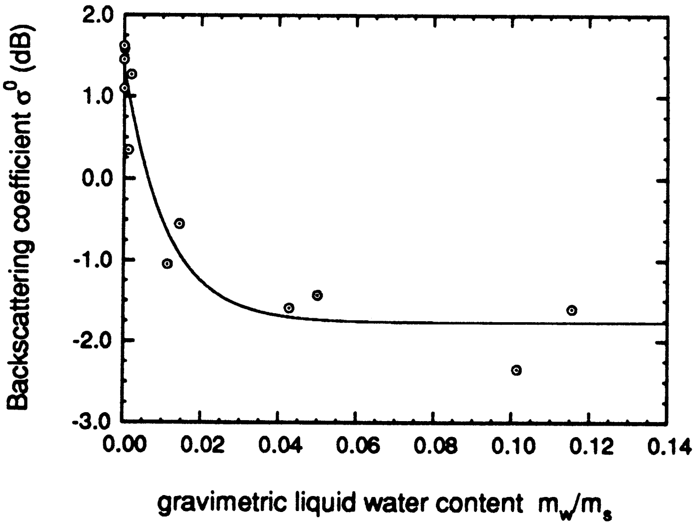

Figure 37: Backscattering coefficient as a function of gravimetric liquid water content for very rough snow at 35 GHz, vv-polarization

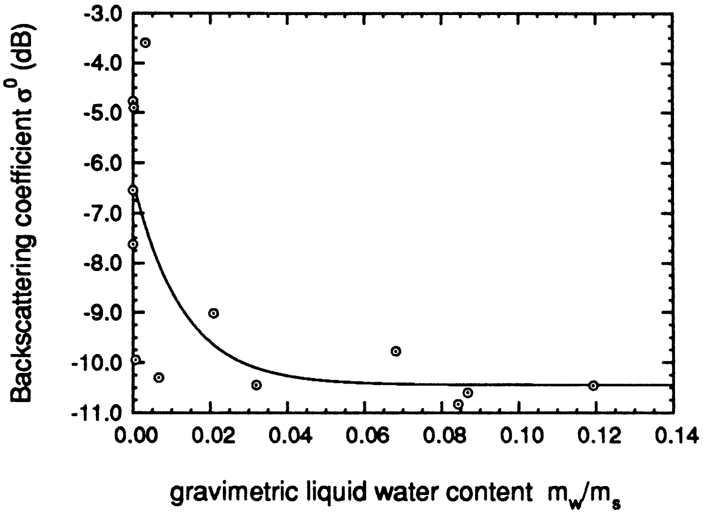

Figure 38: Backscattering coefficient as a function of gravimetric liquid water content for undisturbed snow at 35 GHz, hv-polarization

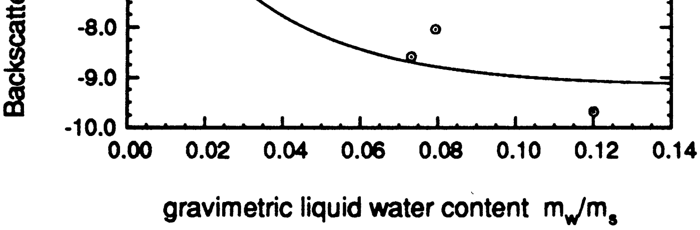

Figure 39: Backscattering coefficient as a function of gravimetric liquid water content for slightly rough snow at 35 GHz, hv-polarization

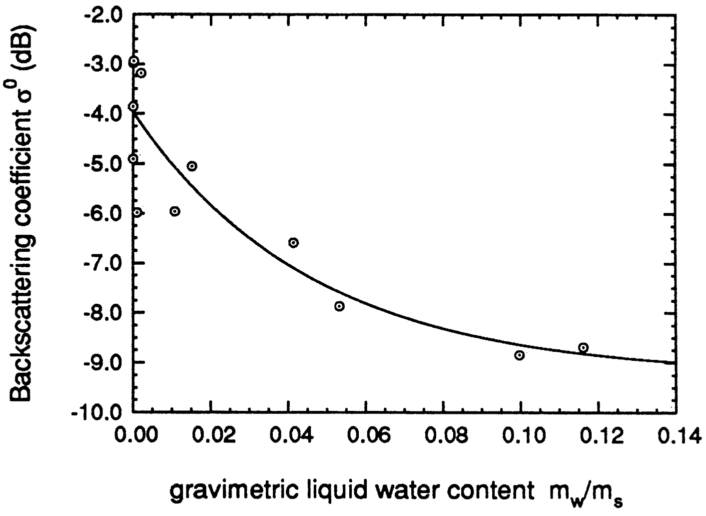

Figure 40: Backscattering coefficient as a function of gravimetric liquid water content for very rough snow at 35 GHz, hv-polarization

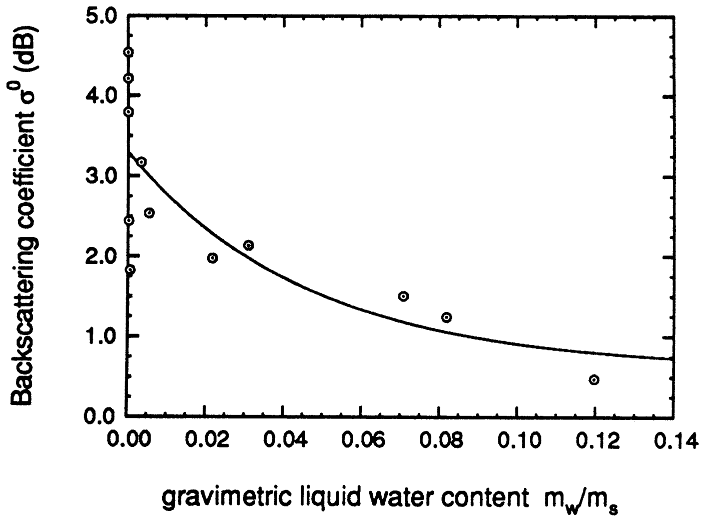

Figure 41: Backscattering coefficient as a function of gravimetric liquid water content for undisturbed snow at 94 GHz, vv-polarization

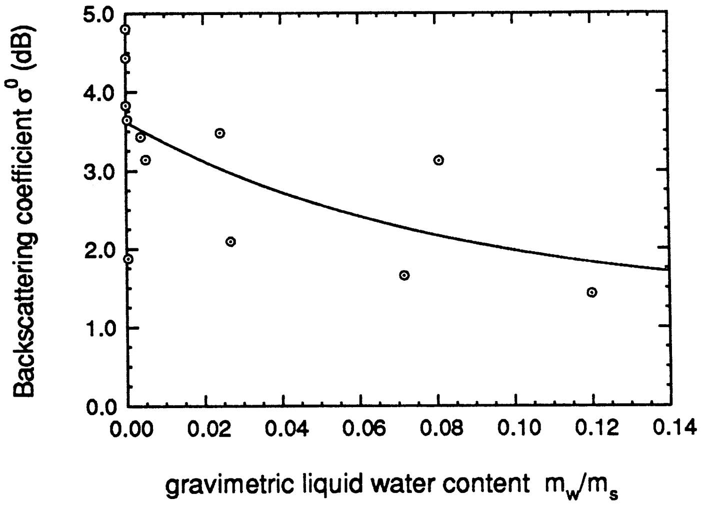

Figure 42: Backscattering coefficient as a function of gravimetric liquid water content for slightly rough snow at 94 GHz, vv-polarization

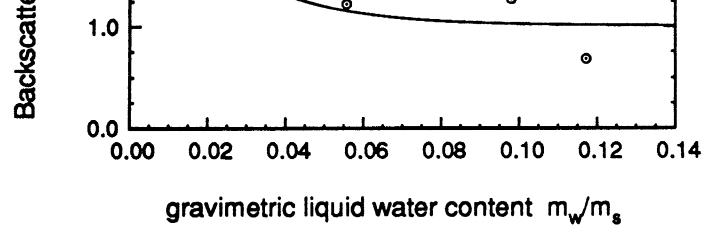

Figure 43: Backscattering coefficient as a function of gravimetric liquid water content for very rough snow at 94 GHz, vv-polarization

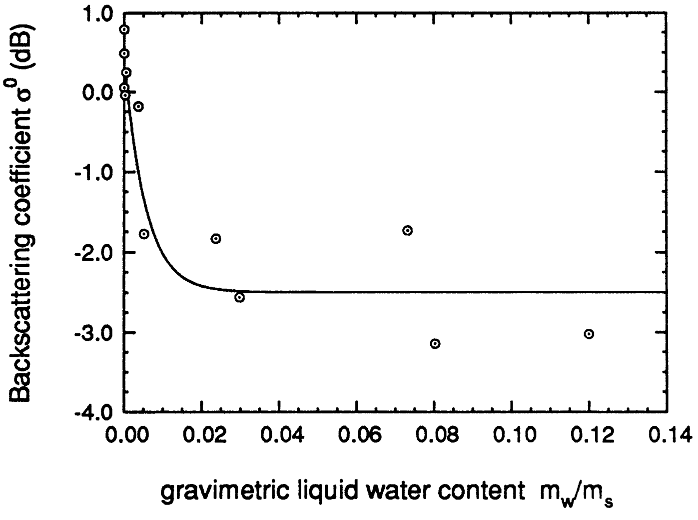

Figure 44: Backscattering coefficient as a function of gravimetric liquid water content for undisturbed snow at 94 GHz, vh-polarization

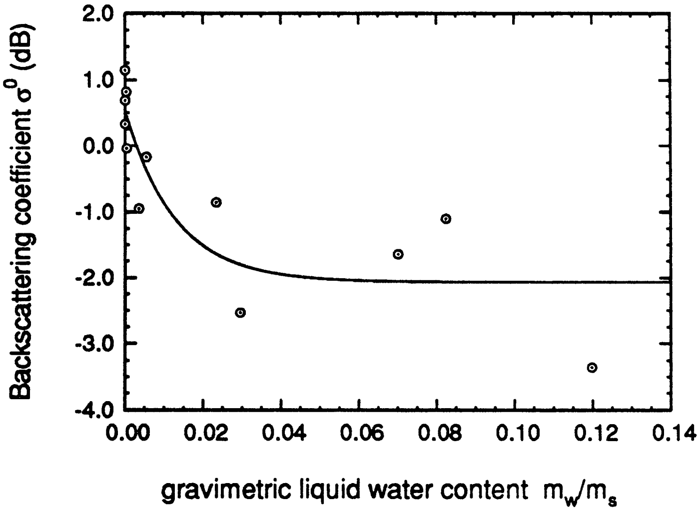

Figure 45: Backscattering coefficient as a function of gravimetric liquid water content for slightly rough snow at 94 GHz, vh-polarization

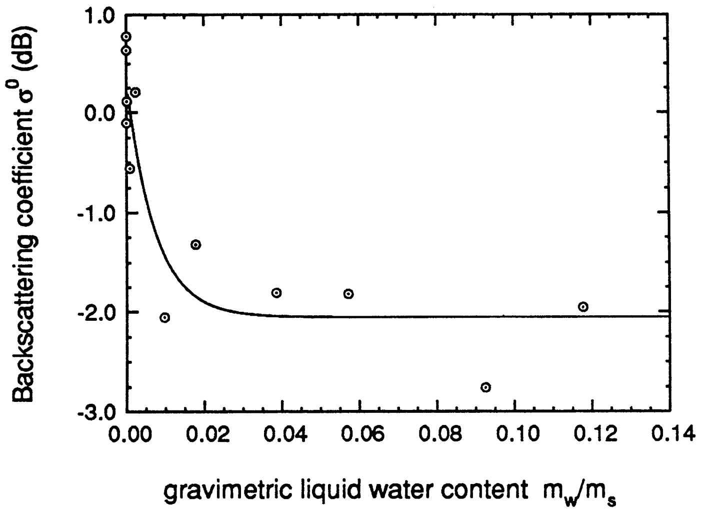

Figure 46: Backscattering coefficient as a function of gravimetric liquid water content for very rough snow at 94 GHz, vh-polarization

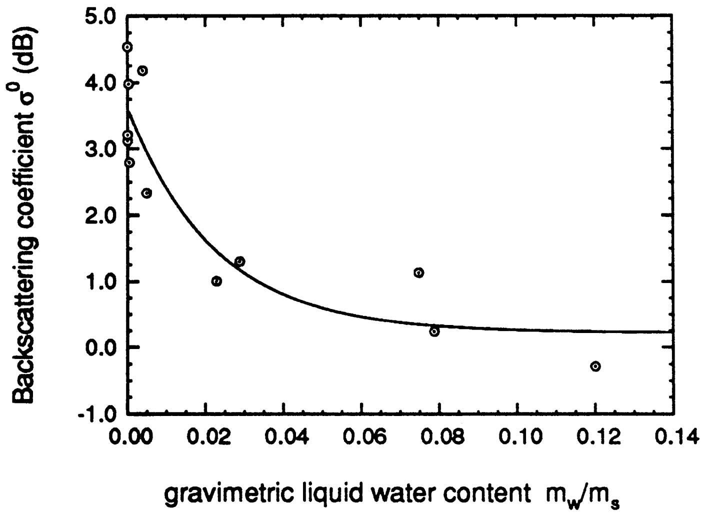

Figure 47: Backscattering coefficient as a function of gravimetric liquid water content for undisturbed snow at 94 GHz, hh-polarization

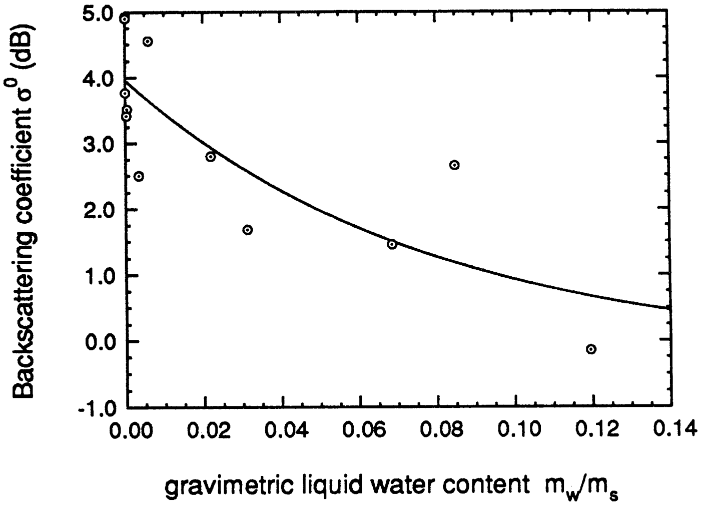

Figure 48: Backscattering coefficient as a function of gravimetric liquid water content for slightly rough snow at 94 GHz, hh-polarization

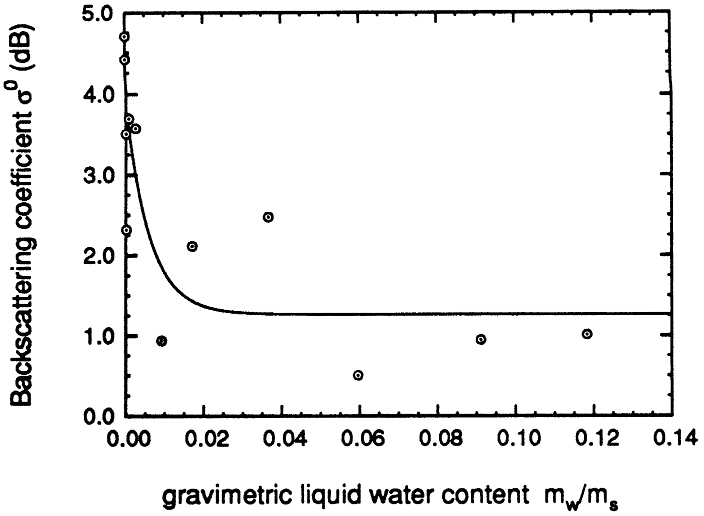

Figure 49: Backscattering coefficient as a function of gravimetric liquid water content for very rough snow at 94 GHz, hh-polarization